

AN ENERGY-STABLE PARAMETRIC FINITE ELEMENT METHOD FOR SIMULATING SOLID-STATE DEWETTING PROBLEMS IN THREE DIMENSIONS

WEIZHU BAO* AND QUAN ZHAO†

Abstract. We propose an accurate and energy-stable parametric finite element method for solving the sharp-interface continuum model of solid-state dewetting in three-dimensional space. The model describes the motion of the film/vapor interface with contact line migration and is governed by the surface diffusion equation with proper boundary conditions at the contact line. We present a new weak formulation for the problem, in which the interface and its contact line are evolved simultaneously. By using piecewise linear elements in space and backward Euler in time, we then discretize the weak formulation to obtain a fully discretized parametric finite element approximation. The resulting numerical method is shown to be well-posed and unconditionally energy-stable. Furthermore, the numerical method is extended for solving the sharp-interface model of solid-state dewetting with anisotropic surface energies in the Riemannian metric form. Numerical results are reported to show the convergence and efficiency of the proposed numerical method as well as the anisotropic effects on the morphological evolution of thin films in solid-state dewetting.

Key words. Solid-state dewetting, surface diffusion, contact line migration, contact angle, parametric finite element method, anisotropic surface energy

AMS subject classifications. 74H15, 74S05, 74M15, 65Z99

1. Introduction. A thin solid film deposited on the substrate agglomerates or dewets to form isolated islands due to surface tension/capillarity effects when heated to high enough temperatures but well below the melting point of the thin film. This process is referred to as the solid-state dewetting (SSD) [40] since the thin film remains solid. In recent years, SSD has been found wide applications in thin film technologies, and it is emerging as a promising route to produce well-controlled patterns of particle arrays used in sensors [29], optical and magnetic devices [37], and catalyst formations [36]. Much experimental (e.g., [43, 44, 1, 35, 17, 32, 27]) and theoretical efforts (e.g., [20, 38, 41, 21, 4, 3, 12, 42, 26, 25]) have been devoted to SSD not just because of its importance in industrial applications but also the arising scientific questions within the problems.

In general, SSD can be regarded as a type of open surface evolution problems governed by surface diffusion [30] and moving contact lines [39]. When the thin film moves along the solid substrate, a moving contact line forms where the three phases (i.e., solid film, vapor and substrate) meet. This brings an additional kinetic feature to this problem. Recently, different mathematical models and simulation methods have been proposed for simulating SSD, such as sharp-interface models [39, 42, 41, 23], phase-field models [20, 15, 31, 19] and other models including the crystalline formulation [11, 47], discrete chemical potential method [12] and kinetic Monte Carlo method [33].

In this work, we restrict ourselves to the model in [23]. It is a sharp-interface model of SSD in three-dimensional (3d) space and was developed based on the thermodynamic variation. As shown in Fig. 1.1, the film/vapor interface is described by an open

*Department of Mathematics, National University of Singapore, Singapore, 119076 (matbaowz@nus.edu.sg). This author's research was supported by the Ministry of Education of Singapore grant MOE2019-T2-1-063 (R-146-000-296-112).

†Department of Mathematics, National University of Singapore, Singapore 119076 (quanzhao90@u.nus.edu). This author's research was supported by the Ministry of Education of Singapore grant R-146-000-285-114.

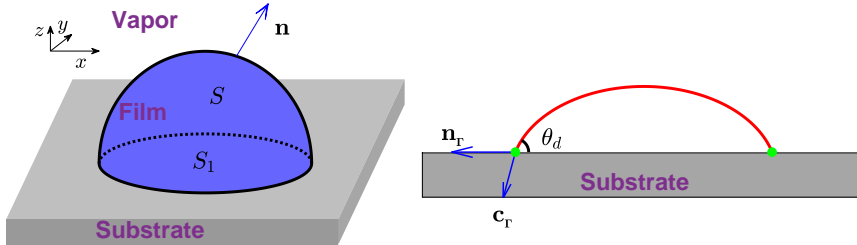


FIG. 1.1. Left panel: An illustration and geometric setup of the solid-state dewetting of thin film (shaded in blue) deposited on a flat rigid substrate (shaded in gray), where S and S_1 represent the film/vapor and the film/substrate interfaces, respectively, and \mathbf{n} is the outward unit normal vector of S . Right panel: configuration of the contact angle: $\theta_d = \arccos(\mathbf{c}_\Gamma \cdot \mathbf{n}_\Gamma)$ at the contact line (green point), where \mathbf{c}_Γ and \mathbf{n}_Γ represent the outward unit conormal vector of S and S_1 , respectively.

surface with parameterization given by (with $\mathbf{X} = (x, y, z)^T$ or $\mathbf{X} = (x_1, x_2, x_3)^T$)

$$(1.1) \quad S(t) := \mathbf{X}(\rho, t) = \left(x_1(\rho, t), x_2(\rho, t), x_3(\rho, t) \right)^T, \quad \rho \in \mathbb{U},$$

where \mathbb{U} is a suitable reference domain. The film/substrate interface is a flat surface and denoted by $S_1(t)$. The two interfaces intersect at the contact line and form a closed curve $\Gamma(t) := S(t) \cap S_1(t)$. We assume $\Gamma(t)$ is a simple closed curve and positively orientated with parameterization given by: $\Gamma(t) := \mathbf{X}_\Gamma(\rho, t)$, $\rho \in \partial\mathbb{U}$. Then the sharp-interface model of SSD in three dimensions can be derived as [23]

$$(1.2a) \quad \partial_t \mathbf{X} = \Delta_s \mathcal{H} \mathbf{n},$$

$$(1.2b) \quad \mathcal{H} = -(\Delta_s \mathbf{X}) \cdot \mathbf{n},$$

where $\mathbf{n} := \mathbf{n}(\mathbf{X}, t)$ and $\mathcal{H} := \mathcal{H}(\mathbf{X}, t)$ represent the unit outward normal vector and the mean curvature of $S(t)$, respectively, and $\Delta_s = \nabla_s \cdot \nabla_s$ is the surface Laplacian operator or Laplace-Beltrami operator. The above equations are supplemented with the following boundary conditions at the moving contact line $\Gamma(t)$ [23]:

(i) contact line condition

$$(1.3) \quad x_3(\cdot, t)|_\Gamma = 0, \quad t \geq 0;$$

(ii) relaxed contact angle condition

$$(1.4) \quad \partial_t \mathbf{X}_\Gamma = -\eta [\mathbf{c}_\Gamma \cdot \mathbf{n}_\Gamma - \cos \theta_i] \mathbf{n}_\Gamma, \quad t \geq 0;$$

(iii) zero-mass flux condition

$$(1.5) \quad (\mathbf{c}_\Gamma \cdot \nabla_s \mathcal{H})|_\Gamma = 0, \quad t \geq 0;$$

where \mathbf{c}_Γ and \mathbf{n}_Γ are the unit outward conormal vectors of $S(t)$ and $S_1(t)$, respectively (see Fig. 1.1), θ_i is the Young's equilibrium angle, and $\eta > 0$ is the contact line mobility which controls the relaxation rate of the dynamical contact angles to the equilibrium contact angle. Condition (i) ensures that the contact line always move along the substrate surface. When $\eta \rightarrow \infty$, condition (ii) collapses to the well-known Young's

equation. Condition (iii) implies that there is no mass-flux at the contact line thus the total mass/volume of the thin film is conserved.

The total energy of the system consists of the film/vapor interfacial energy and the substrate surface energy:

$$(1.6) \quad W(t) := |S(t)| - \cos \theta_i |S_1(t)|,$$

where $|S(t)|$ and $|S_1(t)|$ denote the surface area of $S(t)$ and $S_1(t)$, respectively. Let $\Omega(t)$ be the region enclosed by $S(t)$ and $S_1(t)$, then the dynamic system obeys the conservation law for the total volume (mass) and the dissipation law for the total surface energy [23]

$$(1.7a) \quad \frac{d}{dt} |\Omega(t)| = \int_{S(t)} \Delta_s \mathcal{H} dA \equiv 0, \quad t \geq 0,$$

$$(1.7b) \quad \frac{d}{dt} W(t) = - \int_{S(t)} \|\nabla_s \mathcal{H}\|^2 dA - \eta \int_{\Gamma(t)} [\mathbf{c}_\Gamma \cdot \mathbf{n}_\Gamma - \cos \theta_i]^2 ds \leq 0,$$

where $\|\cdot\|$ is the Euclidean norm in \mathbb{R}^3 .

There exist several numerical methods for simulating interface evolution under surface diffusion as well as its applications in SSD. The main difficulty of the problem arises from the complexity of the high-order and nonlinear governing equations and the possible deterioration of the interface mesh during numerical implementation. Therefore, most front tracking methods, no matter in the framework of finite difference [42, 13, 41, 28] or finite element method [2, 16, 34], generally have to introduce mesh regularization/smoothing algorithms or artificial tangential velocities to prevent the mesh distortion. By reformulating (1.2) into a mixed-type formulation as

$$(1.8a) \quad \mathbf{n} \cdot \partial_t \mathbf{X} = \Delta_s \mathcal{H},$$

$$(1.8b) \quad \mathcal{H} \mathbf{n} = -(\Delta_s \mathbf{X}),$$

Barrett et al. [5, 9] introduced a new variational formulation and designed an elegant semi-implicit parametric finite element method (PFEM) for the surface diffusion equation. The PFEM enjoys a few important and valuable properties including unconditional stability, energy dissipation, and asymptotic mesh equal distribution. It has been successfully extended for solving anisotropic surface diffusion flow under a specific form of convex anisotropies in Riemannian metric form, for simulating the evolution of coupled surface with grain boundary motions and triple junctions [6, 8, 7]. Recently, the PFEM has been extended for solving the sharp interface models of SSD in both 2d and 3d space [4, 22, 46]. However, in those extensions of the PFEM for SSD, they evolve the motions of the interface and the contact lines separately, and do not make full use of the variational structure of the SSD problem. The stability condition depends strongly on the mesh size and the contact line mobility. The convergence rate in space deteriorates and reduces to only first-order.

Motivated by our recent work in 2d space [45], the main aim of this is to propose a new variational formulation and to design an energy-stable parametric finite element method (ES-PFEM) for the 3d SSD problem (1.2) with the boundary conditions (1.3)-(1.5). We first reformulate the relaxed contact angle condition (1.4) into a Robin-type boundary condition such that it can be naturally absorbed into the weak formulation. This novel treatment helps to maintain the unconditional energy stability of the fully discretized scheme. Furthermore, we extend our ES-PFEM for solving

the SSD problem with Riemannian metric type anisotropic surface energies, where the anisotropy is formulated as sums of weighted vector norms [6]. We report the convergence rate of our ES-PFEM and also investigate the anisotropic effects in SSD via different numerical setups.

The rest of the paper is organized as follows. In section 2, we present the novel weak formulation and show that the weak solution satisfies the mass conservation and energy dissipation. In section 3, we propose an ES-PFEM as the full discretization of the weak formulation and show the well-posedness and unconditional energy stability of the numerical method. Subsequently, we extend our numerical method for solving the model of SSD with Riemannian metric type anisotropic surface energies in section 4. Numerical results are reported with convergence test and some applications in section 5. Finally, we draw some conclusions in section 6.

2. A weak formulation. In this section, we first introduce some relevant geometric notations. We then present a weak formulation for the sharp interface model of SSD in (1.8) (and thus (1.2)) with boundary conditions (1.3)-(1.5), and show the mass conservation and energy dissipation within the weak formulation.

2.1. Geometric notations. Suppose $S := S(t) = \mathbf{X}(\cdot, t)$ is a smooth open surface with smooth boundary $\Gamma := \Gamma(t)$. We denote the surface gradient ∇_S over S as a vector operator

$$(2.1) \quad \nabla_S = (\mathbb{I} - \mathbf{n} \otimes \mathbf{n}) \nabla := (\underline{D}_1, \underline{D}_2, \underline{D}_3)^T,$$

where $\mathbb{I} \in \mathbb{R}^{3 \times 3}$ is the identity matrix and \mathbf{n} the unit outward normal vector. In particular, we have

$$(2.2) \quad \underline{D}_i x_j = \delta_{ij} - n_i n_j, \quad 1 \leq i, j \leq 3,$$

where we denote $\mathbf{X} = (x_1, x_2, x_3)^T$, $\mathbf{n} = (n_1, n_2, n_3)^T$, and δ_{ij} is the Kronecker delta function. Finally, the integration by parts formula on $S(t)$ reads [14]

$$(2.3) \quad \int_{S(t)} \underline{D}_i f \, dA = \int_{S(t)} f \mathcal{H} n_i \, dA + \int_{\Gamma(t)} f c_{\Gamma,i} \, ds, \quad \forall f \in C^1(S),$$

where $\mathbf{c}_\Gamma = (c_{\Gamma,1}, c_{\Gamma,2}, c_{\Gamma,3})^T$.

We define the function space $L^2(S(t))$ by

$$(2.4) \quad L^2(S(t)) := \left\{ \psi : S(t) \rightarrow \mathbb{R}, \quad \int_{S(t)} \psi^2 \, dA < \infty \right\},$$

equipped with the L^2 -inner product over $S(t)$

$$(2.5) \quad (u, v)_{S(t)} := \int_{S(t)} u v \, dA, \quad u, v \in L^2(S(t)),$$

and the associated L^2 -norm $\|u\|_{S(t)} := \sqrt{(u, u)_{S(t)}}$. The Sobolev space $H^1(S(t))$ can be naturally defined as

$$(2.6) \quad H^1(S(t)) := \left\{ \psi \in L^2(S(t)), \text{ and } \underline{D}_i \psi \in L^2(S(t)), i = 1, 2, 3 \right\},$$

where $\underline{D}_i f$ is the derivative in weak sense.

On the boundary $\Gamma(t)$, we denote

$$(2.7) \quad (u, v)_{\Gamma(t)} = \int_{\Gamma(t)} u v \, ds.$$

2.2. The formulation. Denote the interface velocity of $S(t)$ as

$$(2.8) \quad \mathbf{v}(\mathbf{X}(\rho, t), t) = \partial_t \mathbf{X}(\rho, t), \quad \forall \mathbf{X} := \mathbf{X}(\rho, t) \in S(t).$$

We define the function space for the interface velocity \mathbf{v} as

$$(2.9) \quad \mathbb{X} := H^1(S(t)) \times H^1(S(t)) \times H_0^1(S(t)),$$

which implies the third component of the velocity on $\Gamma(t)$ is zero during the time evolution.

Multiplying a test function $\psi \in H^1(S(t))$ to (1.8a), integrating over $S(t)$, using integration by parts and the zero-mass flux condition in (1.5), we obtain

$$(2.10) \quad (\mathbf{v} \cdot \mathbf{n}, \psi)_{S(t)} + (\nabla_s \mathcal{H}, \nabla_s \psi)_{S(t)} = 0.$$

For the curvature, we have the following proposition:

PROPOSITION 2.1. $\forall \mathbf{g} = (g_1, g_2, g_3)^T \in [H^1(S(t))]^3$, it holds that

$$(2.11) \quad (\mathcal{H} \mathbf{n}, \mathbf{g})_{S(t)} - (\nabla_s \mathbf{X}, \nabla_s \mathbf{g})_{S(t)} + (\mathbf{c}_\Gamma, \mathbf{g})_{\Gamma(t)} = 0.$$

Proof. Taking the inner product of (1.8b) with a test function $\mathbf{g} = (g_1, g_2, g_3)^T \in [H^1(S(t))]^3$, we obtain

$$(2.12) \quad \begin{aligned} 0 &= (\mathcal{H} \mathbf{n}, \mathbf{g})_{S(t)} + \sum_{i=1}^3 \sum_{j=1}^3 (\underline{D}_i \underline{D}_i x_j, g_j)_{S(t)} \\ &= (\mathcal{H} \mathbf{n}, \mathbf{g})_{S(t)} - \sum_{i=1}^3 \sum_{j=1}^3 (\underline{D}_i x_j, \underline{D}_i g_j)_{S(t)} + \sum_{i=1}^3 \sum_{j=1}^3 (\underline{D}_i x_j g_j, c_{\Gamma,i})_{\Gamma(t)}, \end{aligned}$$

where we have applied the integration by part formula (2.3).

Using the fact $\mathbf{c}_\Gamma \cdot \mathbf{n} = 0$ and (2.2), we can compute the line integral as

$$(2.13) \quad \begin{aligned} \sum_{i=1}^3 \sum_{j=1}^3 (\underline{D}_i x_j g_j, c_{\Gamma,i})_{\Gamma(t)} &= \sum_{i=1}^3 \sum_{j=1}^3 ((\delta_{ij} - n_i n_j) g_j, c_{\Gamma,i})_{\Gamma(t)} \\ &= \sum_{i=1}^3 (g_i, c_{\Gamma,i})_{\Gamma(t)} - \sum_{i=1}^3 \sum_{j=1}^3 (n_j g_j, n_i c_{\Gamma,i})_{\Gamma} = (\mathbf{c}_\Gamma, \mathbf{g})_{\Gamma(t)}. \end{aligned}$$

Combining (2.12) and (2.13), we immediately obtain (2.11). \square

For the relaxed contact angle condition in (1.4), we can reformulate it as

$$(2.14) \quad \mathbf{c}_\Gamma \cdot \mathbf{n}_\Gamma = -\frac{1}{\eta} (\mathbf{v} \cdot \mathbf{n}_\Gamma) \Big|_{\Gamma(t)} + \cos \theta_i.$$

We then decompose the conormal vector as $\mathbf{c}_\Gamma = (\mathbf{c}_\Gamma \cdot \mathbf{e}_z) \mathbf{e}_z + (\mathbf{c}_\Gamma \cdot \mathbf{n}_\Gamma) \mathbf{n}_\Gamma$, where $\mathbf{e}_z = (0, 0, 1)^T$. Choosing $\mathbf{g} \in \mathbb{X}$, then using the decomposition as well as (2.14), we can recast (2.11) as

$$\begin{aligned} 0 &= (\mathcal{H} \mathbf{n}, \mathbf{g})_{S(t)} - (\nabla_s \mathbf{X}, \nabla_s \mathbf{g})_{S(t)} + (\mathbf{c}_\Gamma \cdot \mathbf{n}_\Gamma, \mathbf{g} \cdot \mathbf{n}_\Gamma)_{\Gamma(t)} \\ &= (\mathcal{H} \mathbf{n}, \mathbf{g})_{S(t)} - (\nabla_s \mathbf{X}, \nabla_s \mathbf{g})_{S(t)} - \frac{1}{\eta} (\mathbf{v} \cdot \mathbf{n}_\Gamma, \mathbf{g} \cdot \mathbf{n}_\Gamma)_{\Gamma(t)} + \cos \theta_i (\mathbf{g}, \mathbf{n}_\Gamma)_{\Gamma(t)}, \end{aligned}$$

where we have used the fact $\mathbf{g} \cdot \mathbf{e}_z = 0$ on $\Gamma(t)$ in the first equality.

Collecting these results, we obtain the weak formulation for the sharp-interface model of SSD (1.2) with boundary conditions (1.3)-(1.5): Given an initial interface $S(0)$ with boundary $\Gamma(0)$, we use the velocity equation (2.8) and find the interface velocity $\mathbf{v}(\cdot, t) \in \mathbb{X}$ and the mean curvature $\mathcal{H}(\cdot, t) \in H^1(S(t))$ such that

$$(2.15a) \quad (\mathbf{n} \cdot \mathbf{v}, \psi)_{S(t)} + (\nabla_s \mathcal{H}, \nabla_s \psi)_{S(t)} = 0, \quad \forall \psi \in H^1(S(t)),$$

$$(2.15b) \quad \begin{aligned} (\mathcal{H} \mathbf{n}, \mathbf{g})_{S(t)} - (\nabla_s \mathbf{X}, \nabla_s \mathbf{g})_{S(t)} - \frac{1}{\eta} (\mathbf{v} \cdot \mathbf{n}_\Gamma, \mathbf{g} \cdot \mathbf{n}_\Gamma)_{\Gamma(t)} \\ + \cos \theta_i (\mathbf{n}_\Gamma, \mathbf{g})_{\Gamma(t)} = 0, \quad \forall \mathbf{g} \in \mathbb{X}. \end{aligned}$$

The above weak formulation is an extension of the previous 2d work in Ref. [45] to the 3d space. Similar work for coupled surface or clusters can be found in Refs. [7, 8].

2.3. Volume/mass conservation and energy dissipation. For the weak formulation in (2.15), we have

PROPOSITION 2.2 (Mass conservation and energy dissipation). *Let $(\mathbf{X}, \mathbf{v}, \mathcal{H})$ be the solution of the weak formulation (2.15) and Eq. (2.8). Then the total mass of the thin film is conserved, i.e.,*

$$(2.16) \quad |\Omega(t)| \equiv |\Omega(0)|, \quad t \geq 0,$$

and the total free energy of the system defined in (1.6) is decreasing, i.e.,

$$(2.17) \quad W(t) \leq W(t') \leq W(0) = |S(0)| - \cos \theta_i |S_1(0)|, \quad \forall t \geq t' \geq 0.$$

Proof. Using the Reynolds transport theorem for the moving domains $\Omega(t)$ (see Theorem 33 in [9]), we have

$$\frac{d}{dt} |\Omega(t)| = \int_{S(t)} \mathbf{v} \cdot \mathbf{n} dA, \quad t \geq 0,$$

where we have used the fact that the normal velocity of $S_1(t)$ is zero. Now setting $\psi = 1$ in (2.15a), we immediately obtain

$$\frac{d}{dt} |\Omega(t)| = (\nabla_s \mathcal{H}, \nabla_s 1)_{S(t)} = 0, \quad t \geq 0.$$

Applying the Reynolds transport theorem for the moving manifold $S(t)$ (see Theorem 32 in [9]), we have

$$\frac{d}{dt} |S(t)| := \int_{S(t)} \nabla_s \cdot \mathbf{v} dA = \int_{S(t)} \nabla_s \mathbf{X} : \nabla_s \mathbf{v} dA,$$

where the second equality is a direct result of (2.2). Again, Using the Reynolds transport theorem for the moving 2d domain $S_1(t)$ yields

$$\frac{d}{dt} |S_1(t)| = \int_{\Gamma(t)} \mathbf{n}_\Gamma \cdot \mathbf{v} ds.$$

Combining these results and noting (1.6), we have

$$(2.18) \quad \frac{d}{dt} W(t) = \left(\nabla_s \mathbf{X}, \nabla_s \mathbf{v} \right)_{S(t)} - \cos \theta_i \left(\mathbf{n}_\Gamma, \mathbf{v} \right)_{\Gamma(t)}.$$

Now choosing $\psi = \mathcal{H}$ in (2.15a) and $\mathbf{g} = \mathbf{v}$ in (2.15b) and using (2.18), we obtain

$$\frac{d}{dt} W(t) = - \left(\nabla_s \mathcal{H}, \nabla_s \mathcal{H} \right)_{S(t)} - \frac{1}{\eta} \left(\mathbf{v} \cdot \mathbf{n}_\Gamma, \mathbf{v} \cdot \mathbf{n}_\Gamma \right)_{\Gamma(t)} \leq 0,$$

which immediately implies (2.17). \square

3. Parametric finite element approximation. In this section, we present an energy-stable PFEM (ES-PFEM) as the full discretization of the weak formulation (2.15) by using continuous piecewise linear elements in space and the (semi-implicit) backward Euler method in time. We show the well-posedness and the unconditional energy stability of the full discretization.

3.1. The discretization. Take $\tau > 0$ as the uniform time step size and denote the discrete time levels as $t_m = m\tau$ for $m = 0, 1, \dots$. We then approximate the evolution surface $S(t_m)$ by the polygonal surface mesh S^m with a collection of K vertices $\{\mathbf{q}_k^m\}_{k=1}^K$ and N mutually disjoint non-degenerate triangles

$$(3.1) \quad S^m := \bigcup_{j=1}^N \overline{\sigma_j^m}, \quad m \geq 0.$$

For $1 \leq j \leq N$, we take $\sigma_j^m := \triangle \{\mathbf{q}_{j_1}^m, \mathbf{q}_{j_2}^m, \mathbf{q}_{j_3}^m\}$ to indicate that $\{\mathbf{q}_{j_1}^m, \mathbf{q}_{j_2}^m, \mathbf{q}_{j_3}^m\}$ are the three vertices of σ_j^m and ordered anti-clockwise on the outer surface of S^m . The boundary of S^m is a collection of connected line segments denoted by $\Gamma^m := \sum_{j=1}^{N_\Gamma} \overline{l_j^m}$. Similarly, we take $l_j^m = [\mathbf{p}_{j_1}^m, \mathbf{p}_{j_2}^m]$ to indicate that $\mathbf{p}_{j_1}^m$ and $\mathbf{p}_{j_2}^m$ are the two endpoints of the j th line segment and ordered according to the orientation of the curve Γ^m .

We define the following finite-dimensional spaces over S^m as

$$(3.2a) \quad \mathbb{M}^m := \left\{ \psi \in C(S^m) : \psi|_{\sigma_j^m} \in \mathcal{P}^1(\sigma_j^m), \quad \forall 1 \leq j \leq N \right\},$$

$$(3.2b) \quad \mathbb{M}_0^m := \left\{ \psi \in \mathbb{M}^m : \psi|_{l_j^m} = 0, \quad \forall 1 \leq j \leq N_\Gamma \right\},$$

$$(3.2c) \quad \mathbb{X}^m := \mathbb{M}^m \times \mathbb{M}^m \times \mathbb{M}_0^m,$$

where $\mathcal{P}^k(\sigma_j^m)$ denotes the spaces of all polynomials with degrees at most k on σ_j^m .

With the finite element spaces defined above, we can naturally parameterize S^{m+1} over S^m such that $S^{m+1} := \mathbf{X}^{m+1}(\cdot) \in \mathbb{X}^m$. In particular, $S^m := \mathbf{X}^m(\cdot) \in \mathbb{X}^m$ can be considered as the identity function. Let $\mathbf{n}^m := \mathbf{n}(\mathbf{X}^m)$ be the outward unit normal to S^m . It is a piecewise constant vector-valued function and can be defined as

$$(3.3) \quad \mathbf{n}^m := \sum_{j=1}^n \mathbf{n}_j^m \chi_{\sigma_j^m}, \quad \text{with} \quad \mathbf{n}_j^m = \frac{(\mathbf{q}_{j_2}^m - \mathbf{q}_{j_1}^m) \times (\mathbf{q}_{j_3}^m - \mathbf{q}_{j_1}^m)}{\|(\mathbf{q}_{j_2}^m - \mathbf{q}_{j_1}^m) \times (\mathbf{q}_{j_3}^m - \mathbf{q}_{j_1}^m)\|},$$

where χ is the characteristic function, and \mathbf{n}_j^m is the outward unit normal on triangle $\sigma_j^m := \Delta \{\mathbf{q}_{j_1}^m, \mathbf{q}_{j_2}^m, \mathbf{q}_{j_3}^m\}$. At the boundary Γ^m , we denote by $\mathbf{n}_\Gamma^m := \mathbf{n}_\Gamma(\mathbf{X}^m)$ the outward

unit conormal vector of S_1^m . Then we can compute it at each line segment $l_j^m = [\mathbf{p}_{j_1}^m, \mathbf{p}_{j_2}^m]$ as

$$(3.4) \quad \mathbf{n}_\Gamma^m \Big|_{l_j^m} := \frac{(\mathbf{p}_{j_2}^m - \mathbf{p}_{j_1}^m) \times \mathbf{e}_z}{\|(\mathbf{p}_{j_2}^m - \mathbf{p}_{j_1}^m) \times \mathbf{e}_z\|}, \quad \forall 1 \leq j \leq N_\Gamma.$$

If f, g are two piecewise continuous functions with possible discontinuities across the edges of the triangle element, we define the following mass-lumped inner product to approximate the inner product over $S(t_m)$

$$(3.5) \quad (f, g)_{S^m}^h := \frac{1}{3} \sum_{j=1}^N \sum_{k=1}^3 |\sigma_j^m| f((\mathbf{q}_{j_k}^m)^-) \cdot g((\mathbf{q}_{j_k}^m)^-),$$

where $|\sigma_j^m| = \frac{1}{2} \|(\mathbf{q}_{j_2}^m - \mathbf{q}_{j_1}^m) \times (\mathbf{q}_{j_3}^m - \mathbf{q}_{j_1}^m)\|$ is the surface area of σ_j^m , and $f((\mathbf{q}_{j_k}^m)^-)$ denotes the one-sided limit of $f(\mathbf{q})$ when \mathbf{q} approaches towards $\mathbf{q}_{j_k}^m$ from triangle σ_j^m , i.e., $f((\mathbf{q}_{j_k}^m)^-) = \lim_{\sigma_j^m \ni \mathbf{q} \rightarrow \mathbf{q}_{j_k}^m} f(\mathbf{q})$.

Let $\mathcal{H}^m(\cdot) \in \mathbb{M}^m$ be the numerical solution of the mean curvature at t_m . We propose the following ES-PFEM as the full discretization of the weak formulation (2.15). Given the polygonal surface $S^0 := \mathbf{X}^0(\cdot) \in \mathbb{X}^m$ as a discretization of the initial surface $S(0)$, for $m \geq 0$ we find the evolution surfaces $S^{m+1} := \mathbf{X}^{m+1}(\cdot) \in \mathbb{X}^m$ and the mean curvature $\mathcal{H}^{m+1}(\cdot) \in \mathbb{M}^m$ via solving the following two equations

$$(3.6a) \quad \left(\frac{\mathbf{X}^{m+1} - \mathbf{X}^m}{\tau}, \mathbf{n}^m \psi^h \right)_{S^m}^h + \left(\nabla_s \mathcal{H}^{m+1}, \nabla_s \psi^h \right)_{S^m} = 0, \quad \forall \psi^h \in \mathbb{M}^m,$$

$$(3.6b) \quad \begin{aligned} \left(\mathcal{H}^{m+1} \mathbf{n}^m, \mathbf{g}^h \right)_{S^m}^h - \left(\nabla_s \mathbf{X}^{m+1}, \nabla_s \mathbf{g}^h \right)_{S^m} + \cos \theta_i \left(\mathbf{n}_\Gamma^{m+\frac{1}{2}}, \mathbf{g}^h \right)_{\Gamma^m} \\ - \frac{1}{\eta \tau} \left((\mathbf{X}_\Gamma^{m+1} - \mathbf{X}_\Gamma^m) \cdot \mathbf{n}_\Gamma^m, \mathbf{g}^h \cdot \mathbf{n}_\Gamma^m \right)_{\Gamma^m} = 0, \quad \forall \mathbf{g}^h \in \mathbb{X}^m, \end{aligned}$$

where ∇_s is the surface gradient operator defined on S^m and

$$(3.7) \quad \mathbf{n}_\Gamma^{m+\frac{1}{2}} = \frac{1}{2} (\partial_s \mathbf{X}_\Gamma^m + \partial_s \mathbf{X}_\Gamma^{m+1}) \times \mathbf{e}_z,$$

with s being the arc length parameter of Γ^m . This semi-implicit approximation helps to maintain the energy stability for the substrate energy (see Lemma. 3.1). In practical computation, $\forall f \in \mathbb{M}^m$, we can compute $\nabla_s f$ on a typical triangle $\sigma = \Delta\{\mathbf{q}_k\}_{k=1}^3$ as

$$(3.8) \quad \nabla_s f|_\sigma := f_1 \frac{(\mathbf{q}_3 - \mathbf{q}_2) \times \mathbf{n}}{2|\sigma|} + f_2 \frac{(\mathbf{q}_1 - \mathbf{q}_3) \times \mathbf{n}}{2|\sigma|} + f_3 \frac{(\mathbf{q}_2 - \mathbf{q}_1) \times \mathbf{n}}{2|\sigma|},$$

where $|\sigma| = \|\mathbf{q}_2 - \mathbf{q}_1\| \times \|\mathbf{q}_3 - \mathbf{q}_1\|$, $f_i = f(\mathbf{q}_i)$ for $i = 1, 2, 3$, and $\mathbf{n} = \frac{(\mathbf{q}_2 - \mathbf{q}_1) \times (\mathbf{q}_3 - \mathbf{q}_1)}{2|\sigma|}$.

The proposed numerical method is semi-implicit, i.e. only a linear system needs to be solved at each time step, and thus it is efficient. In addition, it conserves the total volume very well up to the truncation error from the time discretization. Besides, a spatial discretization of (2.15a) by using the piecewise linear elements introduces an implicit tangential velocity of the mesh points and result in the good mesh quality. The detailed investigation of this property has been presented in Ref. [5].

3.2. Well-posedness. Let $\mathcal{J}_k^m := \{1 \leq j \leq N \mid \mathbf{q}_k^m \in \overline{\sigma_j^m}\}$ be the index collection of triangles that contain the vertex \mathbf{q}_k^m , $1 \leq k \leq K$. We define the weighted unit normal at the vertex \mathbf{q}_k^m as

$$(3.9) \quad \boldsymbol{\omega}_k^m := \frac{1}{\sum_{j \in \mathcal{J}_k^m} |\sigma_j^m|} \left(\sum_{j \in \mathcal{J}_k^m} |\sigma_j^m| \mathbf{n}_j^m \right),$$

where \mathbf{n}_j^m is defined in (3.3) as the unit normal of the triangle σ_j^m .

For the discretization in (3.6), we have

THEOREM 3.1 (Existence and uniqueness). *Assume that S^m satisfies:*

(i) $\min_{1 \leq j \leq N} |\sigma_j^m| > 0$;

(ii) *there exist a vertex $\mathbf{q}_{k_0} \in \Gamma^m$ such that $\boldsymbol{\omega}_{k_0}^m = (w_{k_0,1}^m, w_{k_0,2}^m, w_{k_0,3}^m)^T$ satisfies*

$$(w_{k_0,1}^m)^2 + (w_{k_0,2}^m)^2 > 0.$$

If $\cos \theta_i = 0$, i.e., $\theta_i = \frac{\pi}{2}$, then the linear system in (3.6) admits a unique solution.

Proof. It is sufficient to prove the corresponding homogeneous linear system only has zero solution. Therefore we consider the following homogeneous linear system: Find $(\mathbf{X}^h, \mathcal{H}^h) \in (\mathbb{X}^m, \mathbb{M}^m)$ such that $\forall \psi^h \in \mathbb{M}^m, \mathbf{g}^h \in \mathbb{X}^h$

$$(3.10a) \quad \left(\mathbf{X}^h, \mathbf{n}^m \psi^h \right)_{S^m}^h + \left(\nabla_s \mathcal{H}^h, \nabla_s \psi^h \right)_{S^m} = 0,$$

$$(3.10b) \quad \left(\mathcal{H}^h \mathbf{n}^m, \mathbf{g}^h \right)_{S^m}^h - \left(\nabla_s \mathbf{X}^h, \nabla_s \mathbf{g}^h \right)_{S^m} - \frac{1}{\eta \tau} \left(\mathbf{X}_\Gamma^h \cdot \mathbf{n}_\Gamma^m, \mathbf{g}^h \cdot \mathbf{n}_\Gamma^m \right)_{\Gamma^m} = 0.$$

Setting $\psi^h = \mathcal{H}^h$ in (3.10a) and $\mathbf{g}^h = \mathbf{X}^h$ in (3.10b), and combining these two equations, we arrive at

$$\left(\nabla_s \mathcal{H}^h, \nabla_s \mathcal{H}^h \right)_{S^m} + \left(\nabla_s \mathbf{X}^h, \nabla_s \mathbf{X}^h \right)_{S^m} + \frac{1}{\eta \tau} \left(\mathbf{X}_\Gamma^h \cdot \mathbf{n}_\Gamma^m, \mathbf{X}_\Gamma^h \cdot \mathbf{n}_\Gamma^m \right)_{\Gamma^m} = 0.$$

This implies $\mathcal{H}^h = \mathcal{H}^c$ and $\mathbf{X}^h = \mathbf{X}^c$ are constants, and $\mathbf{X}_\Gamma^h \cdot \mathbf{n}_\Gamma^m = 0$. Therefore we have $\mathbf{X}^h \equiv \mathbf{0}$. Plugging \mathcal{H}^c and $\mathbf{X}^c = \mathbf{0}$ into (3.10b), we have

$$(3.11) \quad \mathcal{H}^c \left(\mathbf{g}^h, \mathbf{n}^m \right)_{S^m}^h = 0, \quad \forall \mathbf{g}^h \in \mathbb{X}^m.$$

Now we choose $\mathbf{g}^h \in \mathbb{X}^m$ such that

$$\mathbf{g}^h|_{\mathbf{q}_k^m} = \begin{cases} \left(w_{k_0,1}^m, w_{k_0,2}^m, 0 \right)^T, & k = k_0, \\ \mathbf{0}, & \text{otherwise.} \end{cases}$$

Plugging \mathbf{g}^h into (3.11) and by noting the mass-lumped norm in (3.5), we obtain

$$\begin{aligned} \mathcal{H}^c \left(\mathbf{g}^h, \mathbf{n}^m \right)_{S^m}^h &= \frac{\mathcal{H}^c}{3} \sum_{j \in \mathcal{J}_k^m} \mathbf{g}^h(\mathbf{q}_k^m) |\sigma_j^m| \mathbf{n}_j^m \\ &= \frac{\mathcal{H}^c}{3} \sum_{j \in \mathcal{J}_{k_0}^m} |\sigma_j^m| \left[(w_{k_0,1}^m)^2 + (w_{k_0,2}^m)^2 \right] = 0. \end{aligned}$$

By noting the two assumptions (i) and (ii), we obtain $\mathcal{H}^c = 0$. This shows the homogenous system (3.10) has only zero solution. Thus the numerical scheme (3.6) admits a unique solution. \square

Assumption (i) implies that each triangle element is non-degenerate, and assumption (ii) implies that the weighted normal vector at $\mathbf{q}_{k_0}^m \in \Gamma^m$ is not perpendicular to the substrate surface (xoy -plane). The numerical method (3.6a)-(3.6b) is proved to be well-posed when $\cos \theta_i = 0$. For general case, it is possible to consider the following alternative numerical method:

$$(3.12a) \quad \left(\frac{\mathbf{X}^{m+1} - \mathbf{X}^m}{\tau}, \mathbf{n}^m \psi^h \right)_{S^m}^h + \left(\nabla_S \mathcal{H}^{m+1}, \nabla_S \psi^h \right)_{S^m} = 0, \quad \forall \psi^h \in \mathbb{M}^m,$$

$$(3.12b) \quad \begin{aligned} & \left(\mathcal{H}^{m+1} \mathbf{n}^m, \mathbf{g}^h \right)_{S^m}^h - \left(\nabla_S \mathbf{X}^{m+1}, \nabla_S \mathbf{g}^h \right)_{S^m} + \cos \theta_i \left(\mathbf{n}_\Gamma^m, \mathbf{g}^h \right)_{\Gamma^m} \\ & - \frac{1}{\eta \tau} \left([\mathbf{X}_\Gamma^{m+1} - \mathbf{X}_\Gamma^m] \cdot \mathbf{n}_\Gamma^m, \mathbf{g}^h \cdot \mathbf{n}_\Gamma^m \right)_{\Gamma^m} = 0, \quad \forall \mathbf{g}^h \in \mathbb{X}^m, \end{aligned}$$

which can be shown to be well-posed regardless of θ_i since the relevant boundary term is explicitly valued. However, it seems not possible to prove the unconditional energy stability for (3.12a)-(3.12b).

3.3. Energy dissipation. For $\mathbf{n}_\Gamma^{m+\frac{1}{2}}$ defined in (3.7), we have the following lemma.

LEMMA 3.1. *It holds that*

$$(3.13) \quad |S_1^{m+1}| - |S_1^m| = \left(\mathbf{n}_\Gamma^{m+\frac{1}{2}}, [\mathbf{X}_\Gamma^{m+1} - \mathbf{X}_\Gamma^m] \right)_{\Gamma^m}, \quad m \geq 0,$$

where $|S_1^m|$ denotes the surface area enclosed by the closed plane curve Γ^m on the substrate.

Proof. Denote $\Gamma^m := \mathbf{X}_\Gamma^m(s)$ and $\Gamma^{m+1} := \mathbf{X}_\Gamma^{m+1}(s)$, where $s \in [0, L^m]$ is the arc length parameter of Γ^m . We can compute

$$\begin{aligned} & \left(\mathbf{n}_\Gamma^{m+\frac{1}{2}}, [\mathbf{X}_\Gamma^{m+1} - \mathbf{X}_\Gamma^m] \right)_{\Gamma^m} \\ &= \underbrace{\frac{1}{2} \int_0^{L^m} (\partial_s \mathbf{X}_\Gamma^{m+1} \times \mathbf{e}_z) \cdot \mathbf{X}_\Gamma^{m+1} \, ds}_{\mathcal{A}} - \underbrace{\frac{1}{2} \int_0^{L^m} (\partial_s \mathbf{X}_\Gamma^m \times \mathbf{e}_z) \cdot \mathbf{X}_\Gamma^m \, ds}_{\mathcal{B}} \\ &+ \underbrace{\frac{1}{2} \int_0^{L^m} (\partial_s \mathbf{X}_\Gamma^m \times \mathbf{e}_z) \cdot \mathbf{X}_\Gamma^{m+1} \, ds}_{\mathcal{C}} - \underbrace{\frac{1}{2} \int_0^{L^m} (\partial_s \mathbf{X}_\Gamma^{m+1} \times \mathbf{e}_z) \cdot \mathbf{X}_\Gamma^m \, ds}_{\mathcal{D}}. \end{aligned}$$

Now we can recast the first two terms as

$$(3.14a) \quad \mathcal{A} = \frac{1}{2} \left(\mathbf{n}_\Gamma^{m+1}, \mathbf{X}_\Gamma^{m+1} \right)_{\Gamma^{m+1}} = |S_1^{m+1}|,$$

$$(3.14b) \quad \mathcal{B} = \frac{1}{2} \left(\mathbf{n}_\Gamma^m, \mathbf{X}_\Gamma^m \right)_{\Gamma^m} = |S_1^m|.$$

For the third term, using integration by parts as well as the equality $(\mathbf{a} \times \mathbf{b}) \cdot \mathbf{c} = -(\mathbf{c} \times \mathbf{b}) \cdot \mathbf{a}$, we have

$$(3.15) \quad \mathcal{C} = -\frac{1}{2} \int_0^{L^m} (\mathbf{X}_\Gamma^m \times \mathbf{e}_z) \cdot \partial_s \mathbf{X}_\Gamma^{m+1} \, ds = \mathcal{D}.$$

Collecting these results in (3.14) and (3.15), we obtain (3.13). \square

Denote

$$(3.16) \quad W^m := |S^m| - \cos \theta_i |S_1^m|.$$

Similar to the previous work in [5], we can prove:

THEOREM 3.2. *Let $(\mathbf{X}^{m+1}, \mathcal{H}^{m+1})$ be the numerical solution of (3.6), then the energy is decreasing during the evolution: i.e.,*

$$(3.17) \quad W^{m+1} \leq W^m \leq W^0 = |S^0| - \cos \theta_i |S_1^0|, \quad m \geq 0.$$

Moreover, we have $\forall m \geq 0$,

$$(3.18) \quad \sum_{l=1}^{m+1} \|\nabla_S \mathcal{H}^l\|_{S^{l-1}}^2 + \frac{1}{\eta} \sum_{l=1}^{m+1} \left\| \left(\frac{\mathbf{X}_\Gamma^l - \mathbf{X}_\Gamma^{l-1}}{\tau} \right) \cdot \mathbf{n}_\Gamma^{l-1} \right\|_{\Gamma^{l-1}}^2 \leq \frac{W^0 - W^{m+1}}{\tau},$$

where $\|\cdot\|_{S^l}$ and $\|\cdot\|_{\Gamma^l}$ are the L^2 -norm over S^l and Γ^l , respectively.

Proof. Setting $\psi^h = \tau \mathcal{H}^{m+1}$ in (3.6a) and $\mathbf{g}^h = \mathbf{X}^{m+1} - \mathbf{X}^m$ in (3.6b), combining these two equations yields

$$(3.19) \quad \begin{aligned} & \tau \left(\nabla_S \mathcal{H}^{m+1}, \nabla_S \mathcal{H}^{m+1} \right)_{S^m} + \left(\nabla_S \mathbf{X}^{m+1}, \nabla_S [\mathbf{X}^{m+1} - \mathbf{X}^m] \right)_{S^m} \\ & + \frac{1}{\eta \tau} \left([\mathbf{X}_\Gamma^{m+1} - \mathbf{X}_\Gamma^m] \cdot \mathbf{n}_\Gamma^m, [\mathbf{X}_\Gamma^{m+1} - \mathbf{X}_\Gamma^m] \cdot \mathbf{n}_\Gamma^m \right)_{\Gamma^m} \\ & - \cos \theta_i \left(\mathbf{n}_\Gamma^{m+\frac{1}{2}}, [\mathbf{X}_\Gamma^{m+1} - \mathbf{X}_\Gamma^m] \right)_{\Gamma^m} = 0. \end{aligned}$$

Using the equality $a(a-b) = \frac{1}{2} (a^2 - b^2 + (a-b)^2)$, we get

$$(3.20) \quad \begin{aligned} & \left(\nabla_S \mathbf{X}^{m+1}, \nabla_S [\mathbf{X}^{m+1} - \mathbf{X}^m] \right)_{S^m} \\ & = \frac{1}{2} \|\nabla_S \mathbf{X}^{m+1}\|_{S^m}^2 - \frac{1}{2} \|\nabla_S \mathbf{X}^m\|_{S^m}^2 + \frac{1}{2} \|\nabla_S (\mathbf{X}^{m+1} - \mathbf{X}^m)\|_{S^m}^2 \\ & \geq |S^{m+1}| - |S^m|, \end{aligned}$$

where we have used the fact $\frac{1}{2} \|\nabla_S \mathbf{X}^m\|_{S^m}^2 = |S^m|$, and $\frac{1}{2} \|\nabla_S \mathbf{X}^{m+1}\|_{S^m}^2 \geq |S^{m+1}|$ (see Lemma 2.1 in Ref. [5]). Plugging (3.20) and (3.13) into (3.19) and noting (3.16), we then obtain

$$(3.21) \quad W^{m+1} + \tau \|\nabla_S \mathcal{H}^{m+1}\|_{S^m}^2 + \frac{1}{\eta \tau} \|(\mathbf{X}_\Gamma^{m+1} - \mathbf{X}_\Gamma^m) \cdot \mathbf{n}_\Gamma^m\|_{\Gamma^m}^2 \leq W^m,$$

which immediately implies (3.17).

Reformulating (3.21) as

$$\|\nabla_S \mathcal{H}^l\|_{S^{l-1}}^2 + \frac{1}{\eta} \left\| \left(\frac{\mathbf{X}_\Gamma^l - \mathbf{X}_\Gamma^{l-1}}{\tau} \right) \cdot \mathbf{n}_\Gamma^{l-1} \right\|_{\Gamma^{l-1}}^2 \leq \frac{W^{l-1} - W^l}{\tau}, \quad l \geq 1,$$

summing up for $l = 1, 2, \dots, m+1$, we obtain (3.18). \square

4. For anisotropic surface energies in Riemannian metric form. In this section, we first present the sharp-interface model of SSD with anisotropic surface energies in the Riemannian metric form, and then extend our ES-PFEM for solving the anisotropic model.

4.1. The model and its weak form. In the anisotropic case, the total free energy of the SSD system reads

$$(4.1) \quad W(t) := \int_{S(t)} \gamma(\mathbf{n}) \, dA - \cos \theta_i |S_1(t)|,$$

where $\gamma(\mathbf{n})$ represents the anisotropic surface energy density of the film/vapor interface. In this work we restrict ourselves to the anisotropy given by sums of weighted vector norms as discussed in [6]:

$$(4.2) \quad \gamma(\mathbf{n}) = \sum_{i=1}^L \gamma_i(\mathbf{n}) = \sum_{i=1}^L \sqrt{\mathbf{n}^T G_i \mathbf{n}},$$

where $G_i \in \mathbb{R}^{3 \times 3}$ is symmetric positive definite for $i = 1, \dots, L$. Some typical examples of $\gamma(\mathbf{n})$ are: (1) isotropic surface energy: $L = 1$, $G_1 = \mathbb{I}$, which gives $\gamma(\mathbf{n}) \equiv 1$; (2) ellipsoidal surface energy: $L = 1$, $G_1 = \text{diag}(a_1^2, a_2^2, a_3^2)$, which gives the ellipsoidal surface energy

$$(4.3) \quad \gamma(\mathbf{n}) = \sqrt{\sum_{i=1}^3 a_i^2 n_i^2}, \quad a_i > 0;$$

and (3) “cubed” surface energy: $L = 3$, $G_1 = \text{diag}(1, \delta^2, \delta^2)$, $G_2 = \text{diag}(\delta^2, 1, \delta^2)$, $G_3 = \text{diag}(\delta^2, \delta^2, 1)$, which gives the “cubed” surface energy

$$(4.4) \quad \gamma(\mathbf{n}) = \sum_{i=1}^3 \sqrt{(1 - \delta^2) n_i^2 + \delta^2 \|\mathbf{n}\|^2}.$$

In fact, (4.4) is a smooth regularization of $\gamma(\mathbf{n}) = \sum_{i=1}^3 |n_i|$ by introducing a small parameter $0 < \delta \ll 1$. For other choices of L and G_i , readers can refer to Ref. [6] and references therein.

Now given the parametrization of the film/vapor interface $\mathbf{X}(\cdot, t)$ in (1.1), the sharp interface model of SSD with anisotropic surface energies can be derived as [23]

$$(4.5a) \quad \partial_t \mathbf{X} = \Delta_s \mu \, \mathbf{n}, \quad t \geq 0,$$

$$(4.5b) \quad \mu = \nabla_s \cdot \boldsymbol{\xi}, \quad \boldsymbol{\xi}(\mathbf{n}) = \sum_{i=1}^L \frac{1}{\gamma_i(\mathbf{n})} G_i \, \mathbf{n},$$

where $\mu(\mathbf{X}, t)$ is the chemical potential and $\boldsymbol{\xi}(\mathbf{n})$ is the associated Cahn-Hoffman $\boldsymbol{\xi}$ -vector [18, 10]. The above equations are supplemented with the contact line condition in (1.3) and the following two addition boundary conditions at the contact line $\Gamma(t)$:

(ii') relaxed anisotropic contact angle condition

$$(4.6) \quad \partial_t \mathbf{X}_\Gamma = -\eta [\mathbf{c}_\Gamma^\gamma \cdot \mathbf{n}_\Gamma - \cos \theta_i] \, \mathbf{n}_\Gamma, \quad t \geq 0;$$

(iii') anisotropic zero-mass flux condition

$$(4.7) \quad (\mathbf{c}_\Gamma \cdot \nabla_s \mu)|_\Gamma = 0, \quad t \geq 0;$$

where \mathbf{c}_Γ^γ is the anisotropic conormal vector defined as

$$\mathbf{c}_\Gamma^\gamma = (\boldsymbol{\xi} \cdot \mathbf{n}) \mathbf{c}_\Gamma - (\boldsymbol{\xi} \cdot \mathbf{c}_\Gamma) \mathbf{n}.$$

When $\eta \rightarrow \infty$, Eq. (4.6) will reduce to the anisotropic Young's equation: $\mathbf{c}_\Gamma^\gamma \cdot \mathbf{n}_\Gamma - \cos \theta_i = 0$.

Before we present the novel weak formulation for the above anisotropic model, we follow the notations in [6] and define the anisotropic surface gradient associated with the symmetric positive matrix $\tilde{G} = (\det G)^{-\frac{1}{2}} G$ as

$$(4.8) \quad \nabla_S^{\tilde{G}} f(\mathbf{X}) = \sum_{i=1}^2 (\partial_{\mathbf{t}_i} f)(\mathbf{X}) \mathbf{t}_i, \quad f(\mathbf{X}) \in H^1(S), \quad \mathbf{X} \in S,$$

where $\partial_{\mathbf{t}_i} f = \mathbf{t}_i \cdot (\nabla_S f)$ is the directional derivative, and $\{\mathbf{t}_1, \mathbf{t}_2\}$ is the orthogonal basis of the tangential space of $S(t)$ with respect to \tilde{G} at the point of interest \mathbf{X} , i.e.,

$$(4.9) \quad \mathbf{t}_i \cdot (\tilde{G} \mathbf{t}_j) = \delta_{ij}, \quad \mathbf{t}_i \cdot \mathbf{n}(\mathbf{X}) = 0, \quad i, j = 1, 2.$$

Moreover, given a vector-valued smooth function \mathbf{g} , the anisotropic surface divergence and anisotropic surface gradient are then defined respectively as

$$(4.10a) \quad (\nabla_S^{\tilde{G}} \cdot \mathbf{g})(\mathbf{X}) = \sum_{i=1}^2 (\partial_{\mathbf{t}_i} \mathbf{g})(\mathbf{X}) \cdot (\tilde{G} \mathbf{t}_i),$$

$$(4.10b) \quad (\nabla_S^{\tilde{G}} \mathbf{g})(\mathbf{X}) = \sum_{i=1}^2 (\partial_{\mathbf{t}_i} \mathbf{g})(\mathbf{X}) \otimes (\tilde{G} \mathbf{t}_i).$$

Then the chemical potential $\mu = \nabla_S \cdot \boldsymbol{\xi}$ can be reformulated as

$$(4.11) \quad \mu \mathbf{n} = \sum_{i=1}^L \gamma_i(\mathbf{n}) \tilde{G}_i \Delta_S^{\tilde{G}_i} \mathbf{X},$$

where $\Delta_S^{\tilde{G}_i} = \nabla_S^{\tilde{G}_i} \cdot \nabla_S^{\tilde{G}_i}$ is the anisotropic surface Laplace-Beltrami operator.

We have the following proposition for the formulation of the chemical potential.

PROPOSITION 4.1. *It holds that*

$$(4.12) \quad \begin{aligned} & (\mu \mathbf{n}, \mathbf{g})_{S(t)} - \sum_{i=1}^L \left(\gamma_i(\mathbf{n}), (\nabla_S^{\tilde{G}_i} \mathbf{X}, \nabla_S^{\tilde{G}_i} \mathbf{g})_{\tilde{G}_i} \right)_{S(t)} + (\mathbf{c}_\Gamma^\gamma, \mathbf{g})_{\Gamma(t)} \\ & = 0, \quad \forall \mathbf{g} = (g_1, g_2, g_3)^T \in [H^1(S(t))]^3, \end{aligned}$$

where we define the inner product with respect to the matrix \tilde{G}

$$(4.13) \quad (\nabla_S^{\tilde{G}} \mathbf{u}, \nabla_S^{\tilde{G}} \mathbf{v})_{\tilde{G}} = \sum_{i=1}^2 (\partial_{\mathbf{t}_i} \mathbf{u}, \partial_{\mathbf{t}_i} \mathbf{v})_{\tilde{G}} = \sum_{i=1}^2 \partial_{\mathbf{t}_i} \mathbf{u} \cdot (\tilde{G} \partial_{\mathbf{t}_i} \mathbf{v}).$$

Proof. The proof of (4.12) is similar to the proof of the proposition 2.1. It can be obtained by taking the inner product of (4.11) with the vector-valued function \mathbf{g} and using integration by parts. Another proof of (4.12) by using the variational approach can be found in Lemma 2.1 in Ref. [7]. The details are omitted here for brevity. \square

In a similar manner as the isotropic case, we choose $\mathbf{g} \in \mathbb{X}$, and use the decomposition of $\mathbf{c}_\Gamma^\gamma = (\mathbf{c}_\Gamma^\gamma \cdot \mathbf{e}_z) \mathbf{e}_z + (\mathbf{c}_\Gamma^\gamma \cdot \mathbf{n}_\Gamma) \mathbf{n}_\Gamma$ and the relaxed anisotropic contact angle

condition in (4.6). As a consequence, (4.12) can be recast as

$$\begin{aligned} 0 &= \left(\mu \mathbf{n}, \mathbf{g} \right)_{S(t)} - \sum_{i=1}^L \left(\gamma_i(\mathbf{n}), \left(\nabla_S^{\tilde{G}_i} \mathbf{X}, \nabla_S^{\tilde{G}_i} \mathbf{g} \right)_{\tilde{G}_i} \right)_{S(t)} + \left(\mathbf{c}_\Gamma \cdot \mathbf{n}_\Gamma, \mathbf{g} \cdot \mathbf{n}_\Gamma \right)_{\Gamma(t)} \\ &= \left(\mu \mathbf{n}, \mathbf{g} \right)_{S(t)} - \sum_{i=1}^L \left(\gamma_i(\mathbf{n}), \left(\nabla_S^{\tilde{G}_i} \mathbf{X}, \nabla_S^{\tilde{G}_i} \mathbf{g} \right)_{\tilde{G}_i} \right)_{S(t)} \\ &\quad - \frac{1}{\eta} \left(\partial_t \mathbf{X}_\Gamma \cdot \mathbf{n}_\Gamma, \mathbf{g} \cdot \mathbf{n}_\Gamma \right)_{\Gamma(t)} + \cos \theta_i \left(\mathbf{n}_\Gamma, \mathbf{g} \right)_{\Gamma(t)}. \end{aligned}$$

Collecting these results, we propose the weak formulation for the sharp-interface model of SSD in (4.5) with boundary conditions (1.3) and (4.6)-(4.7): given the initial surface $S(0)$ with contact line $\Gamma(0) = \partial S(0)$, for $t > 0$ we seek the interface velocity $\mathbf{v}(\cdot, t) \in \mathbb{X}$ and the chemical potential $\mu(\cdot, t) \in H^1(S(t))$ via solving the following two equations

$$(4.14a) \quad \left(\mathbf{v} \cdot \mathbf{n}, \psi \right)_{S(t)} + \left(\nabla_S \mu, \nabla_S \psi \right)_{S(t)} = 0, \quad \forall \psi \in H^1(S(t)),$$

$$\begin{aligned} (4.14b) \quad &\left(\mu \mathbf{n}, \mathbf{g} \right)_{S(t)} - \sum_{i=1}^L \left(\gamma_i(\mathbf{n}), \left(\nabla_S^{\tilde{G}_i} \mathbf{X}, \nabla_S^{\tilde{G}_i} \mathbf{g} \right)_{\tilde{G}_i} \right)_{S(t)} \\ &- \frac{1}{\eta} \left(\mathbf{v} \cdot \mathbf{n}_\Gamma, \mathbf{g} \cdot \mathbf{n}_\Gamma \right)_{\Gamma(t)} + \cos \theta_i \left(\mathbf{n}_\Gamma, \mathbf{g} \right)_{\Gamma(t)} = 0, \quad \forall \mathbf{g} \in \mathbb{X}, \end{aligned}$$

together with the velocity equation in (2.8).

The mass conservation and energy dissipation within the weak formulation can be easily established in a similar manner as in section 2.3.

4.2. The ES-PFEM and its properties. Following the discretization in section 3.1, we propose an ES-PFEM as the full discretization of the weak formulation in (4.14) as follows: Given the polygonal surface $S^0 := \mathbf{X}^0(\cdot) \in \mathbb{X}^m$, for $m \geq 0$ we find the evolution surfaces $S^{m+1} := \mathbf{X}^{m+1}(\cdot) \in \mathbb{X}^m$ and the chemical potential $\mu^{m+1}(\cdot) \in \mathbb{M}^m$ via solving the following two equations

$$(4.15a) \quad \left(\frac{\mathbf{X}^{m+1} - \mathbf{X}^m}{\tau}, \mathbf{n}^m \psi^h \right)_{S^m}^h + \left(\nabla_S \mu^{m+1}, \nabla_S \psi^h \right)_{S^m} = 0, \quad \forall \psi^h \in \mathbb{M}^m,$$

$$\begin{aligned} (4.15b) \quad &\left(\mu^{m+1} \mathbf{n}^m, \mathbf{g}^h \right)_{S^m}^h - \sum_{i=1}^L \left(\gamma_i(\mathbf{n}^m), \left(\nabla_S^{\tilde{G}_i} \mathbf{X}^{m+1}, \nabla_S^{\tilde{G}_i} \mathbf{g}^h \right)_{\tilde{G}_i} \right)_{S^m} \\ &+ \cos \theta_i \left(\mathbf{n}_\Gamma^{m+\frac{1}{2}}, \mathbf{g}^h \right)_{\Gamma^m} - \frac{1}{\eta \tau} \left([\mathbf{X}_\Gamma^{m+1} - \mathbf{X}_\Gamma^m] \cdot \mathbf{n}_\Gamma^m, \mathbf{g}^h \cdot \mathbf{n}_\Gamma^m \right)_{\Gamma^m} \\ &= 0, \quad \forall \mathbf{g}^h \in \mathbb{X}^m, \end{aligned}$$

where ∇_S and $\nabla_S^{\tilde{G}_i}$ are defined on S^m , and $\mathbf{n}_\Gamma^{m+\frac{1}{2}}$ is defined in (3.7). In practical computation, $\forall f \in \mathbb{M}^m$, $\nabla_S f$ can be computed via (3.8). Furthermore, $\nabla_S^{\tilde{G}} f$ on a typical triangle $\sigma = \Delta\{\mathbf{q}_k\}_{k=1}^3$ are computed by using the definition (4.8) as

$$\nabla_S^{\tilde{G}} f|_\sigma := (\nabla_S f \cdot \mathbf{t}_1) \mathbf{t}_1 + (\nabla_S f \cdot \mathbf{t}_2) \mathbf{t}_2,$$

where \mathbf{t}_1 and \mathbf{t}_2 are parallel to the triangle σ and satisfy (4.9). In the case when $L = 1$ and $G_1 = \mathbb{I}$, the numerical scheme in (4.15) reduces to the scheme in (3.6).

For the discretization in (4.15), similar to the proof of Theorem 3.1 (with details omitted for brevity), we have:

THEOREM 4.1 (Existence and uniqueness). *Assume that S^m satisfies:*

(i) $\min_{1 \leq j \leq N} |\sigma_j^m| > 0$;

(ii) *there exists a vertex $\mathbf{q}_{k_0} \in \Gamma^m$ such that $\boldsymbol{\omega}_{k_0}^m = (w_{k_0,1}^m, w_{k_0,2}^m, w_{k_0,3}^m)^T$ satisfies*

$$(w_{k_0,1}^m)^2 + (w_{k_0,2}^m)^2 > 0$$
.

If $\cos \theta_i = 0$, i.e. $\theta_i = \frac{\pi}{2}$, then the linear system in (4.15) admits a unique solution.

Denote

$$(4.16) \quad W^m := \int_{S^m} \gamma(\mathbf{n}^m) dA - \cos \theta_i |S_1^m| = \sum_{j=1}^N \gamma(\mathbf{n}_j^m) |\sigma_j^m| - \cos \theta_i |S_1^m|,$$

where $\gamma(\mathbf{n})$ is defined in (4.2). Similar to the previous work in [6], we can prove:

THEOREM 4.2. *Let $(\mathbf{X}^{m+1}, \mu^{m+1})$ be the numerical solution of (4.15), then the total energy of the system is decreasing during the evolution, i.e.,*

$$(4.17) \quad W^{m+1} \leq W^m \leq W^0 = \sum_{j=1}^N \gamma(\mathbf{n}_j^0) |\sigma_j^0| - \cos \theta_i |S_1^0|, \quad \forall m \geq 0.$$

Moreover, we have $\forall m \geq 0$,

$$(4.18) \quad \sum_{l=1}^{m+1} \|\nabla_S \mu^l\|_{S^{l-1}}^2 + \frac{1}{\eta} \sum_{l=1}^{m+1} \left\| \left(\frac{\mathbf{X}_\Gamma^l - \mathbf{X}_\Gamma^{l-1}}{\tau} \right) \cdot \mathbf{n}_\Gamma^{l-1} \right\|_{\Gamma^{l-1}}^2 \leq \frac{W^0 - W^{m+1}}{\tau}.$$

Proof. Setting $\psi^h = \mu^{m+1}$ in (4.15a) and $\mathbf{g}^h = \mathbf{X}^{m+1} - \mathbf{X}^m$ in (4.15b), and combining these two equations we obtain

$$(4.19) \quad \begin{aligned} & \tau \left(\nabla_S \mu^{m+1}, \nabla_S \mu^{m+1} \right)_{S^m} - \cos \theta_i \left(\mathbf{n}_\Gamma^{m+\frac{1}{2}}, [\mathbf{X}_\Gamma^{m+1} - \mathbf{X}_\Gamma^m] \right)_{\Gamma^m} \\ & + \sum_{i=1}^L \left(\gamma_i(\mathbf{n}^m), \left(\nabla_S^{\tilde{G}_i} \mathbf{X}^{m+1}, \nabla_S^{\tilde{G}_i} (\mathbf{X}^{m+1} - \mathbf{X}^m) \right)_{\tilde{G}_i} \right)_{S^m} \\ & + \frac{1}{\eta \tau} \left([\mathbf{X}_\Gamma^{m+1} - \mathbf{X}_\Gamma^m] \cdot \mathbf{n}_\Gamma^m, [\mathbf{X}_\Gamma^{m+1} - \mathbf{X}_\Gamma^m] \cdot \mathbf{n}_\Gamma^m \right)_{\Gamma^m} = 0. \end{aligned}$$

Using the equality $a(a-b) = \frac{1}{2} (a^2 - b^2 + (a-b)^2)$, we obtain

$$(4.20) \quad \begin{aligned} & \left(\gamma_i(\mathbf{n}^m), \left(\nabla_S^{\tilde{G}_i} \mathbf{X}^{m+1}, \nabla_S^{\tilde{G}_i} (\mathbf{X}^{m+1} - \mathbf{X}^m) \right)_{\tilde{G}_i} \right)_{S^m} \\ & = \frac{1}{2} \left(\gamma_i(\mathbf{n}^m), \left\| \nabla_S^{\tilde{G}_i} \mathbf{X}^{m+1} \right\|_{\tilde{G}_i}^2 - \left\| \nabla_S^{\tilde{G}_i} \mathbf{X}^m \right\|_{\tilde{G}_i}^2 + \left\| \nabla_S^{\tilde{G}_i} (\mathbf{X}^{m+1} - \mathbf{X}^m) \right\|_{\tilde{G}_i}^2 \right)_{S^m} \\ & \geq \int_{S^{m+1}} \gamma_i(\mathbf{n}^{m+1}) dA - \int_{S^m} \gamma_i(\mathbf{n}^m) dA, \end{aligned}$$

where $\|\cdot\|_{\tilde{G}}$ is the induced norm of the inner product in (4.13), and the last inequality is obtained by using the fact (see Lemma 3.1 in Ref. [6])

$$(4.21a) \quad \frac{1}{2} \left(\gamma_i(\mathbf{n}^m), \left\| \nabla_s^{\tilde{G}_i} \mathbf{X}^{m+1} \right\|_{\tilde{G}} \right)_{S^m} \geq \int_{S^{m+1}} \gamma_i(\mathbf{n}^{m+1}) \, dA,$$

$$(4.21b) \quad \frac{1}{2} \left(\gamma_i(\mathbf{n}^m), \left\| \nabla_s^{\tilde{G}_i} \mathbf{X}^m \right\|_{\tilde{G}} \right)_{S^m} = \int_{S^m} \gamma_i(\mathbf{n}^m) \, dA.$$

Now substituting (4.20), (4.2) and (4.16) into (4.19), and also noting the equality (3.13), we obtain

$$(4.22) \quad W^{m+1} + \tau \left\| \nabla_s \mu^{m+1} \right\|_{S^m}^2 + \frac{1}{\eta \tau} \left\| (\mathbf{X}_{\Gamma}^{m+1} - \mathbf{X}_{\Gamma}^m) \cdot \mathbf{n}_{\Gamma}^m \right\|_{\Gamma^m}^2 \leq W^m, \quad m \geq 0.$$

Reformulating (4.22) as

$$\left\| \nabla_s \mu^l \right\|_{S^{l-1}}^2 + \frac{1}{\eta} \left\| \left(\frac{\mathbf{X}_{\Gamma}^l - \mathbf{X}_{\Gamma}^{l-1}}{\tau} \right) \cdot \mathbf{n}_{\Gamma}^{l-1} \right\|_{\Gamma^{l-1}}^2 \leq \frac{W^{l-1} - W^l}{\tau}, \quad l \geq 1,$$

summing up for $l = 1, 2, \dots, m+1$, we obtain (4.18). \square

5. Numerical results. In this section, we first present the convergence tests of our numerical method in (3.6) and (4.15), and then report some numerical examples to demonstrate the morphological features of SSD in 3d space. The resulting linear system in (3.6) and (4.15) can be efficiently solved via the Schur complement method discussed in [5] or simply GMRES method with preconditioners based on incomplete LU factorization. The contact line mobility η in (1.4) controls the relaxation rate of the dynamic contact angle to the equilibrium angle, and large η accelerates the relaxation process [41, 46]. In the following simulations, we will always choose $\eta = 100$ unless otherwise stated.

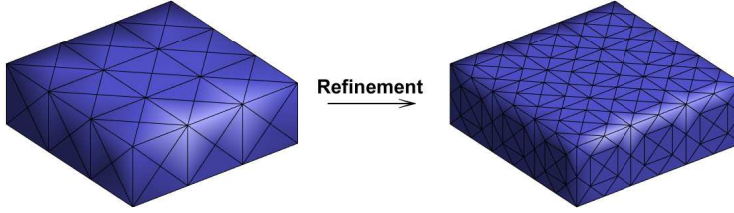


FIG. 5.1. Interface partition of a (3,3,1) cuboid with mesh size $h = 0.5$ (left panel), and a refined polygonal surface with mesh size $h = 0.25$ (right panel) obtained by subdividing each triangle into 4 smaller triangles.

5.1. Convergence tests. We test the convergence rate of the numerical methods in (3.6) and (4.15) by carrying out numerical simulations under different mesh sizes and time step sizes. Initially, the island film is chosen as a cuboid island with (3,3,1) representing its length, width and height. The region occupied by the initial thin film is then given by $[-1.5, 1.5] \times [-1.5, 1.5] \times [0, 1]$. Let $S^0 := \bigcup_{j=1}^N \overline{\sigma_j^0}$ be the initial partition of $S(0)$ and $\mathbf{X}_{h,\tau}^m(\cdot)$ be the numerical solution of the interface $S(t_m)$ obtained using mesh size $h = \max_{j=1}^N \sqrt{|\sigma_j^0|}$ and time step size τ . Then we measure the error of the numerical solutions by comparing $\mathbf{X}_{h,\tau}^m$ and $\mathbf{X}_{\frac{h}{2}, \frac{\tau}{4}}^m$.

To measure the difference between two polygonal surfaces given by

$$(5.1a) \quad S := \bigcup_{j=1}^N \overline{\sigma_j} \quad \text{with vertices } \{\mathbf{q}_k\}_{k=1}^K,$$

$$(5.1b) \quad S' = \bigcup_{j=1}^{N'} \overline{\sigma'_j} \quad \text{with vertices } \{\mathbf{q}'_k\}_{k=1}^{K'},$$

we define the following manifold distance

$$(5.2) \quad \mathcal{M}(S, S') = \frac{1}{2} \left(\max_{1 \leq k \leq K'} \min_{1 \leq j \leq N} \text{dist}(\mathbf{q}'_k, \sigma_j) + \max_{1 \leq k \leq K} \min_{1 \leq j \leq N'} \text{dist}(\mathbf{q}_k, \sigma'_j) \right),$$

where $\text{dist}(\mathbf{q}, \sigma) = \inf_{\mathbf{p} \in \sigma} \|\mathbf{p} - \mathbf{q}\|$ represents the distance of the vertex \mathbf{q} to the triangle σ in the 3d space.

We fix $\theta_i = 2\pi/3$ and consider the isotropic case and anisotropic case by choosing the ellipsoidal surface energies in (4.3) with $a_1 = 2, a_2 = 1, a_3 = 1$. We then compute the numerical error based on the manifold distance in (5.2) by

$$(5.3) \quad e_{h,\tau}(t_m) := \mathcal{M}(\mathbf{X}_{h,\tau}^m, \mathbf{X}_{\frac{h}{2}, \frac{\tau}{4}}^m), \quad m \geq 0.$$

Numerical errors for the two cases are reported in Table 5.1. We observe that the error decreases with refined mesh size and time step size, and the order of convergence can reach about 2 for spatial discretization.

TABLE 5.1

Error $e_{h,\tau}$ and the rate of convergence for the dynamic interface under the isotropic surface energy (upper panel) and the ellipsoidal surface energy (4.3) with $a_1 = 2, a_2 = 1, a_3 = 1$ (lower panel) at three different times. Other parameters are chosen as $\theta_i = 2\pi/3$, $h_0 = 0.5$ and $\tau_0 = 0.01$.

(h, τ)	$e_{h,\tau}(t = 0.5)$	order	$e_{h,\tau}(t = 1.0)$	order	$e_{h,\tau}(t = 2.0)$	order
(h_0, τ_0)	8.17E-2	-	7.19E-2	-	6.61E-2	-
$(\frac{h_0}{2}, \frac{\tau_0}{2})$	2.05E-2	1.99	1.71E-2	2.07	1.71E-2	1.95
$(\frac{h_0}{2^2}, \frac{\tau_0}{2^4})$	4.80E-3	2.07	4.85E-3	1.82	5.20E-3	1.72

(h, τ)	$e_{h,\tau}(t = 0.5)$	order	$e_{h,\tau}(t = 1.0)$	order	$e_{h,\tau}(t = 2.0)$	order
(h_0, τ_0)	8.03E-2	-	7.93E-2	-	7.85E-2	-
$(\frac{h_0}{2}, \frac{\tau_0}{2})$	2.03E-2	1.98	2.15E-2	1.88	2.25E-2	1.80
$(\frac{h_0}{2^2}, \frac{\tau_0}{2^4})$	5.31E-3	1.93	5.46E-3	2.09	5.45E-3	2.05

TABLE 5.2

Numerical errors between the numerical equilibrium contact angle (at time $t = 10$) and the Young's angle θ_i for isotropic surface energy, where $h_0 = 0.5, \tau_0 = 0.01$.

(h, τ)	$\theta_i = \pi/2$		$\theta_i = 2\pi/3$	
	$ \theta - \theta_i (t = 10)$	order	$ \theta - \theta_i (t = 10)$	order
(h_0, τ_0)	1.00E-1	-	2.03E-1	-
$(\frac{h_0}{2}, \frac{\tau_0}{2})$	5.70E-2	0.81	1.10E-1	0.88
$(\frac{h_0}{2^2}, \frac{\tau_0}{2^4})$	2.90E-2	0.97	5.72E-2	0.95
$(\frac{h_0}{2^3}, \frac{\tau_0}{2^6})$	1.44E-2	1.05	2.98E-2	0.94

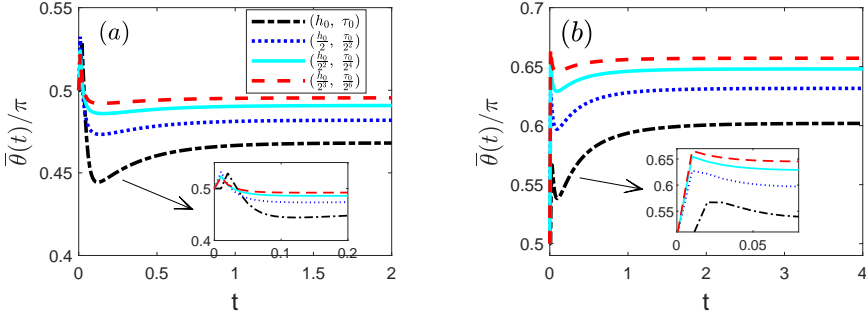


FIG. 5.2. The time history of the average contact angle defined in (5.4) by using different mesh sizes and time step sizes, where $h_0 = 0.5$ and $\tau_0 = 0.01$. (a) $\theta_i = \pi/2$; (b) $\theta_i = 2\pi/3$.

To further assess the accuracy of the numerical method in (3.6), we define the following average contact angle $\bar{\theta}$

$$(5.4) \quad \bar{\theta}|_{t=t_m} := \frac{1}{N_\Gamma} \sum_{j=1}^{N_\Gamma} \arccos \left(\mathbf{c}_{\Gamma,j}^m \cdot \mathbf{n}_{\Gamma,j}^m \right),$$

where $\mathbf{c}_{\Gamma,j}^m$ and $\mathbf{n}_{\Gamma,j}^m$ are numerical approximations of \mathbf{c}_Γ and \mathbf{n}_Γ at j th line segment of Γ^m , respectively. The time history of the average contact angles computed using different mesh sizes and time step sizes for $\theta_i = \pi/2$ and $\theta_i = 2\pi/3$ are presented in Fig. 5.2. We observe the convergence of the dynamic contact angle as the mesh is refined. A more quantitative assessment for the average contact angle $\bar{\theta}$ is provided in Table. 5.2, where we show the error between $\bar{\theta}$ for the equilibrium state ($t = 10$) and the Young's angle θ_i . We observe the error decreases as mesh is refined, and the convergence rate for $|\bar{\theta} - \theta_i|$ is about 1.

5.2. Applications. We present some numerical examples to demonstrate the anisotropic effects on the morphological evolution of thin films in SSD.

Example 1. In this example, we consider the evolution of square island films under: (1) isotropic surface energy $\gamma(\mathbf{n}) = 1$; (2) ellipsoidal surface energy in (4.3) with $a_1 = 2, a_2 = 1, a_3 = 1$; and (3) “cuboid” surface energy in (4.4) with $\delta = 0.1$. The initial film is chosen as a $(3.2, 3.2, 0.1)$ cuboid island. The interface is partitioned into $N = 18432$ triangles with $K = 9345$ vertices, and we take $\tau = 1 \times 10^{-4}$, $\theta_i = 2\pi/3$.

Several snapshots of the morphological evolutions for the thin film under the three anisotropies are shown in Fig. 5.3, 5.4 and 5.5, respectively. In the isotropic case, we observe the four corners of the square island retract much more slowly than that of the four edges at the beginning, thus forming a cross-shaped geometry. As time evolves, the island finally forms a perfectly spherical shape as equilibrium. For ellipsoidal surface energy, the square island forms a grooved shape and then reach an ellipsoidal shape as equilibrium. In the case of “cuboid” surface energy, the island maintains a self-similar cuboid shape by gradually decreasing its length, width and increasing its height until reaching the equilibrium state.

In Fig. 5.6, we plot the temporal evolution of the normalized energy $W(t)/W(0)$ and the relative volume loss ΔV defined as

$$(5.5) \quad \Delta V := \frac{V^h(t) - V^h(0)}{|V^h(0)|}, \quad t \geq 0,$$

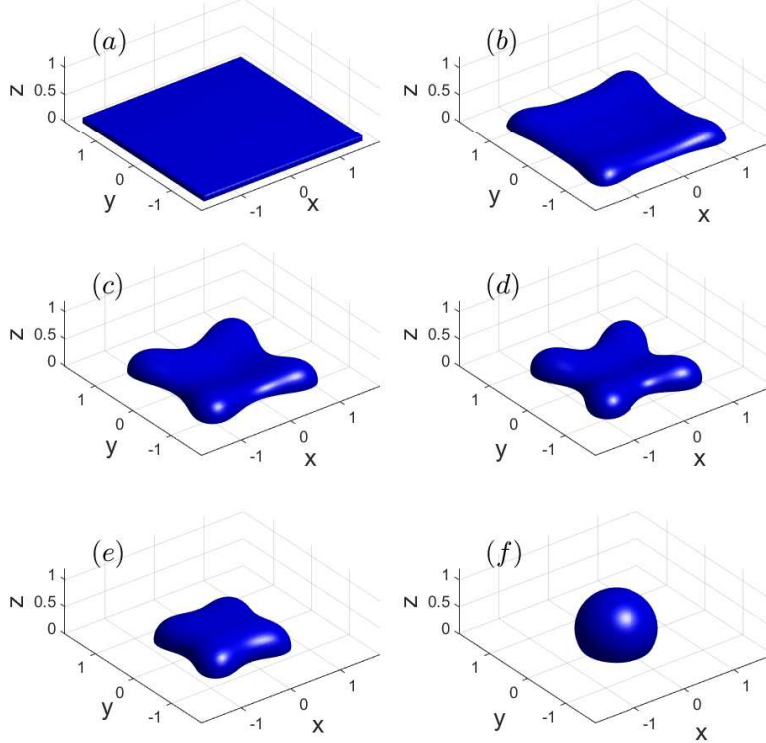


FIG. 5.3. Several snapshots in the evolution of an initially square island film towards its equilibrium shape under the isotropic surface energy: (a) $t = 0$; (b) $t = 0.004$; (c) $t = 0.008$; (d) $t = 0.012$; (e) $t = 0.020$; (f) $t = 0.080$. The initial shape is chosen as a (3.2, 3.2, 0.1) cuboid, and $\theta_i = 2\pi/3$.

where $V^h(0)$ is the total volume of the initial shape. We observe the total free energy of the discrete system decays in time, and the relative volume loss is about 1% to 2%.

Example 2. We investigate the equilibrium shapes of SSD by using different θ_i and surface energies. We consider the “cursed” surface energy defined in (4.4) with four different rotations: (1) $\gamma(\mathbf{n})$ defined in (4.4) with $\delta = 0.1$; (2) $\gamma(\mathbf{R}_x(\pi/4)\mathbf{n})$; (3) $\gamma(\mathbf{R}_y(\pi/4)\mathbf{n})$; (4) $\gamma(\mathbf{R}_z(\pi/4)\mathbf{n})$, where $\mathbf{R}_x(\pi/4)$, $\mathbf{R}_y(\pi/4)$ and $\mathbf{R}_z(\pi/4)$ represent the orthogonal matrix for the rotation by an angle $\pi/4$ about the x,y,z-axis using the right-hand rule, respectively. The initial thin film is chosen as a (3,3,1) cuboid island. The interface is partitioned into $N = 5376$ triangles with $K = 2737$ vertices, and $\tau = 10^{-2}$.

As it can be seen from Fig. 5.7(a)-(c), θ_i controls the equilibrium contact angle and thus the equilibrium shape. From Fig. 5.7(d)-(f), we observe that a rotation of the “cursed” anisotropy will result in a corresponding rotation of the equilibrium shape.

Example 3. We examine the geometric evolution of the square-ring patch under the “cursed” surface energies used in Fig. 5.7(c)-(f). The initial island is chosen as a (12,12,1) cuboid by cutting out a (10, 10, 1) cuboid from the centre. The interface is partitioned into $N = 33792$ triangles with $K = 17248$ vertices, and we take $\tau = 2 \times 10^{-4}$, $\theta_i = 2\pi/3$.

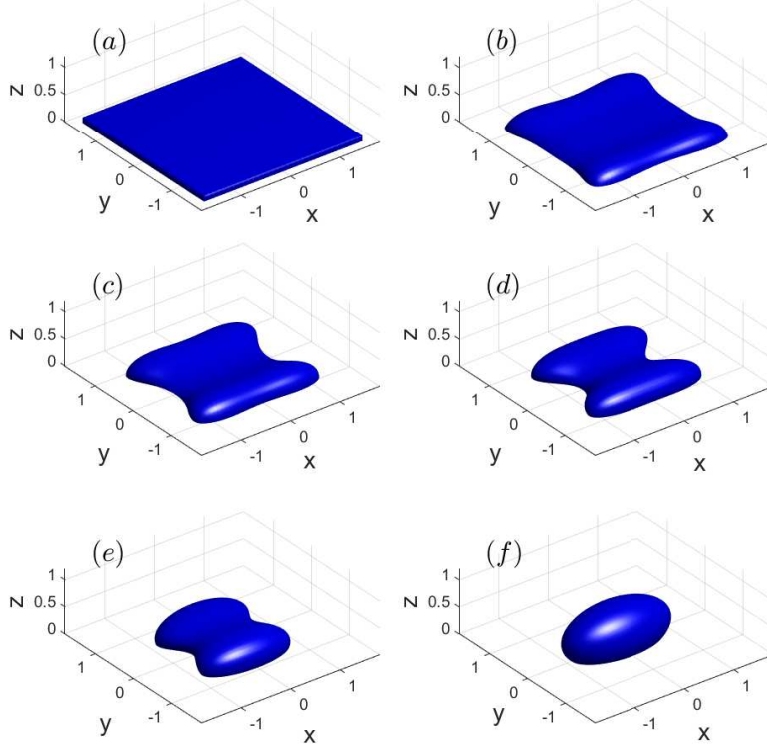


FIG. 5.4. Several snapshots in the evolution of an initially square island film towards its equilibrium shape under the ellipsoidal surface energy: (a) $t = 0$; (b) $t = 0.004$; (c) $t = 0.008$; (d) $t = 0.012$; (e) $t = 0.020$; (f) $t = 0.080$. The initial shape is chosen as a (3.2, 3.2, 0.1) cuboid, and $\theta_i = 2\pi/3$. The surface energy is chosen in (4.3) with $a_1 = 2, a_2 = 1, a_3 = 1$.

The geometric evolutions for the square-ring island are shown in Fig. 5.8 -5.11 for the four cases, respectively. When the surface energy density is given by (4.4), we observe that the thin square-ring patch gradually shrinks towards the centre to form a self-similar square-ring shape. When the orientation of the anisotropy is rotated with respect to x -axis by $\pi/4$, we observe from Fig. 5.9 that a break-up of the island along the y -direction occurs. Similarly, a rotation of the anisotropy with respect to y -axis results in the breakup of the island along x -axis, as expected in Fig. 5.10. Furthermore, we observe that when the orientation of the anisotropy is rotated with respect to the z -axis, the square-ring forms several isolated particles.

It is well-known in isotropic case, the Rayleigh-like instability in the azimuthal direction and the shrinking instability in the radial direction are competing with each other to determine the geometric evolution of a square-ring island [24, 46]. Generally, a very thin square island always breaks up into isolated particles since the Rayleigh-like instability dominates the kinetic evolution; while for a fat square-ring island, the shrinking instability dominates the evolution and makes the island shrink towards the center. Our numerical simulations indicate that anisotropic surface energies play an important role in the evolution of the square-ring island. They can either enhance or mitigate the Rayleigh-like instability in the azimuthal direction, thus producing a variety of morphological evolutions.

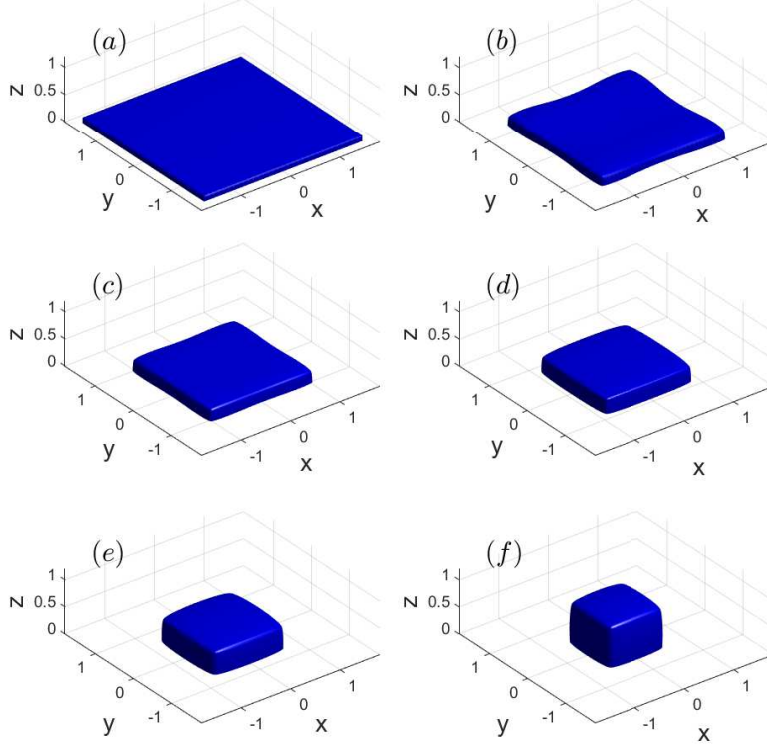


FIG. 5.5. Several snapshots in the evolution of an initially square island film towards its equilibrium shape under the “cusped” surface energy: (a) $t = 0$; (b) $t = 0.004$; (c) $t = 0.008$; (d) $t = 0.012$; (e) $t = 0.020$; (f) $t = 0.080$, where the initial shape is chosen as a $(3.2, 3.2, 0.1)$ cuboid, and $\theta_i = 2\pi/3$. The surface energy is chosen in (4.4) with $\delta = 0.1$.

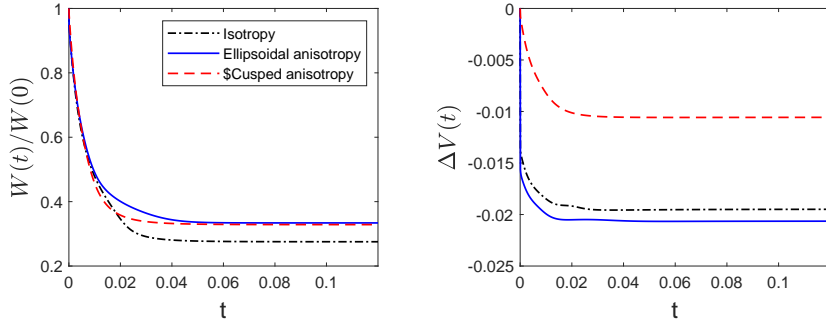


FIG. 5.6. The temporal evolution of the normalized energy $W(t)/W(0)$ (left panel) and the relative volume loss $\Delta V(t)$ (right panel) by using the isotropic surface energy, the ellipsoidal surface energy and cusped surface energy.

6. Conclusions. We developed an efficient, accurate, and energy-stable parametric finite element method (ES-PFEM) for solving the sharp-interface model of solid-state dewetting in both the isotropic case and the anisotropic case with anisotropic surface energies in the Riemannian metric form. By reformulating the relaxed con-

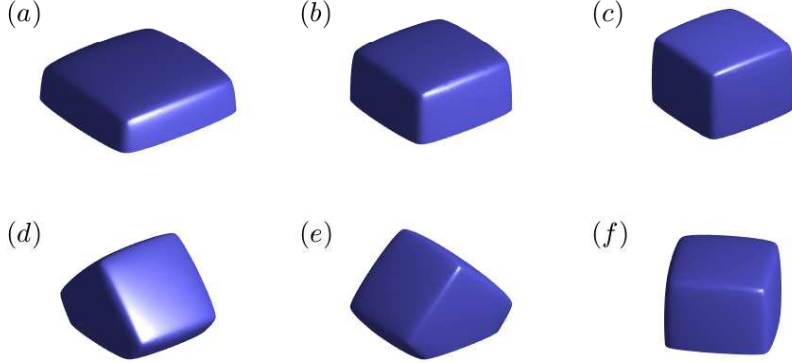


FIG. 5.7. The equilibrium profiles of the island film obtained using different θ_i and anisotropies. For (a)-(c), we fix $\gamma(\mathbf{n})$ in (4.4) with $\delta = 0.1$, and $\theta_i = \pi/3, \pi/2, 2\pi/3$, respectively. For (d)-(f), we set $\theta_i = 2\pi/3$ but choose $\gamma(\mathbf{R}_x(\pi/4)\mathbf{n})$, $\gamma(\mathbf{R}_y(\pi/4)\mathbf{n})$ and $\gamma(\mathbf{R}_z(\pi/4)\mathbf{n})$, respectively.

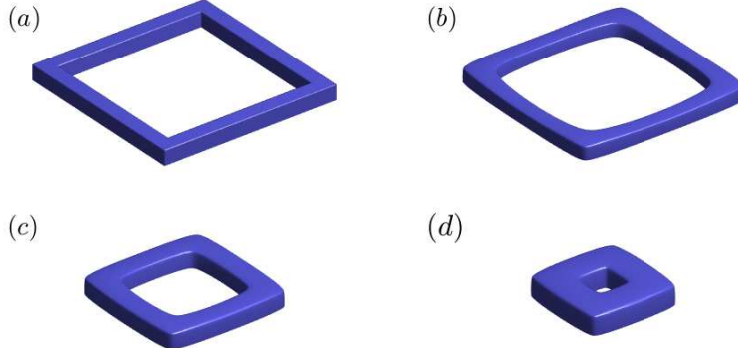


FIG. 5.8. Snapshots of the island film in the evolution of an initially square-ring patch with $\theta_i = 2\pi/3$. The surface energy is given by (4.4) with $\delta = 0.1$. (a) $t = 0$; (b) $t = 1.0$; (c) $t = 8.0$; (d) $t = 12.6$.

tact angle condition as a time-dependent Robin-type of boundary condition for the interface, we obtained a new weak formulation. By using continuous piecewise linear elements in space and the backward Euler method in time, we then discretized the weak formulation to obtain the semi-implicit ES-PFEM. We rigorously proved the well-posedness and unconditional energy stability of the numerical method. We assessed the accuracy and convergence of the proposed ES-PFEM and found that it can attain the second-order convergence rate of the spatial error for the dynamic interface and the first-order convergence rate of the contact angle for the equilibrium interface. Finally, we investigated the anisotropic effects on the evolution of large square islands and square-ring islands by using different anisotropic surface energies. In fact, the proposed ES-PFEM provides a nice tool for simulating different applications in solid-state dewetting in three dimensions.

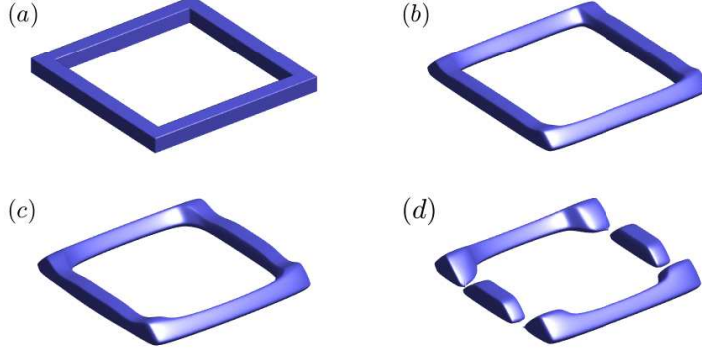


FIG. 5.9. Snapshots of the island film in the evolution of an initially square-ring patch with $\theta_i = 2\pi/3$. The surface energy is given by $\gamma(\mathbf{R}_x(\pi/4) \mathbf{n})$, where $\gamma(\mathbf{n})$ is defined in (4.4) with $\delta = 0.1$. (a) $t = 0$; (b) $t = 0.1$; (c) $t = 0.5$; (d) $t = 1.12$.

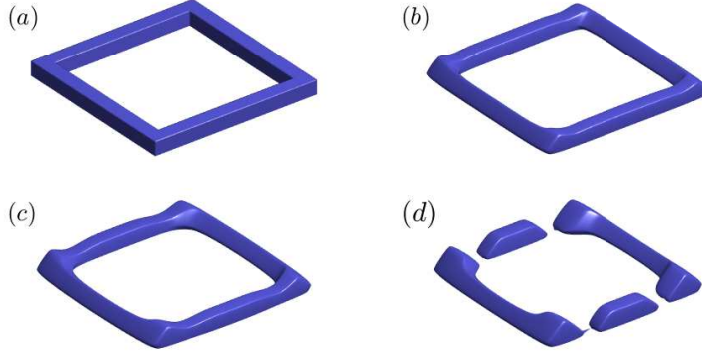


FIG. 5.10. Snapshots of the island film in the evolution of an initially square-ring patch with $\theta_i = 2\pi/3$. The surface energy is chosen as $\gamma(\mathbf{R}_y(\pi/4) \mathbf{n})$, where $\gamma(\mathbf{n})$ is defined in (4.4) with $\delta = 0.1$. (a) $t = 0$; (b) $t = 0.1$; (c) $t = 0.5$; (d) $t = 1.12$.

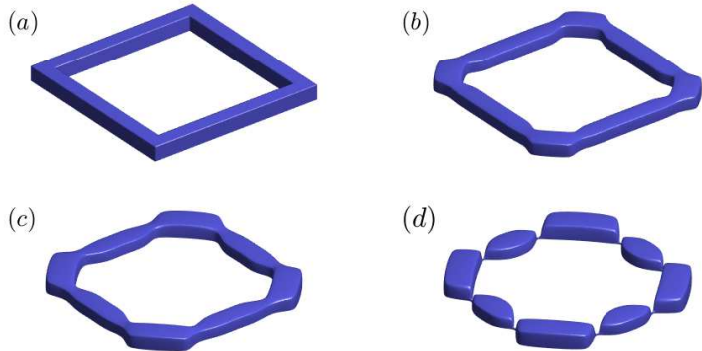


FIG. 5.11. Snapshots of the island film in the evolution of an initially square-ring patch with $\theta_i = 2\pi/3$. The surface energy is given by $\gamma(\mathbf{R}_z(\pi/4) \mathbf{n})$, where $\gamma(\mathbf{n})$ is defined in (4.4) with $\delta = 0.1$. (a) $t = 0$; (b) $t = 0.1$; (c) $t = 0.4$; (d) $t = 0.76$.

REFERENCES

- [1] D. AMRAM, L. KLINGER, AND E. RABKIN, *Anisotropic hole growth during solid-state dewetting of single-crystal Au–Fe thin films*, *Acta Mater.*, 60 (2012), pp. 3047–3056.
- [2] E. BÄNSCH, P. MORIN, AND R. H. NOCHETTO, *A finite element method for surface diffusion: the parametric case*, *J. Comput. Phys.*, 203 (2005), pp. 321–343.
- [3] W. BAO, W. JIANG, D. J. SROLOVITZ, AND Y. WANG, *Stable equilibria of anisotropic particles on substrates: a generalized Winterbottom construction*, *SIAM J. Appl. Math.*, 77 (2017), pp. 2093–2118.
- [4] W. BAO, W. JIANG, Y. WANG, AND Q. ZHAO, *A parametric finite element method for solid-state dewetting problems with anisotropic surface energies*, *J. Comput. Phys.*, 330 (2017), pp. 380–400.
- [5] J. W. BARRETT, H. GARCKE, AND R. NÜRNBERG, *On the parametric finite element approximation of evolving hypersurfaces in \mathbb{R}^3* , *J. Comput. Phys.*, 227 (2008), pp. 4281–4307.
- [6] J. W. BARRETT, H. GARCKE, AND R. NÜRNBERG, *A variational formulation of anisotropic geometric evolution equations in higher dimensions*, *Numer. Math.*, 109 (2008), pp. 1–44.
- [7] J. W. BARRETT, H. GARCKE, AND R. NÜRNBERG, *Finite-element approximation of coupled surface and grain boundary motion with applications to thermal grooving and sintering*, *Eur. J. Appl. Math.*, 21 (2010), pp. 519–556.
- [8] J. W. BARRETT, H. GARCKE, AND R. NÜRNBERG, *Parametric approximation of surface clusters driven by isotropic and anisotropic surface energies*, *Interface Free Bound.*, 12 (2010), pp. 187–234.
- [9] J. W. BARRETT, H. GARCKE, AND R. NÜRNBERG, *Parametric finite element approximations of curvature driven interface evolutions*, *Handb. Numer. Anal.* (Andrea Bonito and Ricardo H. Nochetto, eds.), 21 (2020), pp. 275–423.
- [10] J. CAHN AND D. HOFFMAN, *A vector thermodynamics for anisotropic surfaces: I. curved and faceted surfaces*, *Acta Metall.*, 22 (1974), pp. 1205–1214.
- [11] W. C. CARTER, A. R. ROOSE, J. W. CAHN, AND J. E. TAYLOR, *Shape evolution by surface diffusion and surface attachment limited kinetics on completely faceted surfaces*, *Acta Metall. Mater.*, 43 (1995), pp. 4309–4323.
- [12] E. DORNEL, J. BARBE, F. DE CRÉCY, G. LACOLLE, AND J. EYMER, *Surface diffusion dewetting of thin solid films: Numerical method and application to Si/SiO₂*, *Phys. Rev. B*, 73 (2006), p. 115427.
- [13] P. DU, M. KHENNER, AND H. WONG, *A tangent-plane marker-particle method for the computation of three-dimensional solid surfaces evolving by surface diffusion on a substrate*, *J. Comput. Phys.*, 229 (2010), pp. 813–827.
- [14] G. DZIUK AND C. M. ELLIOTT, *Finite element methods for surface PDEs*, *Acta Numer.*, 22 (2013), pp. 289–396.
- [15] M. DZIWNIK, A. MÜNCH, AND B. WAGNER, *An anisotropic phase-field model for solid-state dewetting and its sharp-interface limit*, *Nonlinearity*, 30 (2017), pp. 1465–1496.
- [16] F. HAUSSER AND A. VOIGT, *A discrete scheme for parametric anisotropic surface diffusion*, *J. Sci. Comput.*, 30 (2007), pp. 223–235.
- [17] A. HERZ, A. FRANZ, F. THESKA, M. HENTSCHEL, T. KUPS, D. WANG, AND P. SCHAAF, *Solid-state dewetting of single-and bilayer Au–W thin films: Unraveling the role of individual layer thickness, stacking sequence and oxidation on morphology evolution*, *AIP Adv.*, 6 (2016), p. 035109.
- [18] D. W. HOFFMAN AND J. W. CAHN, *A vector thermodynamics for anisotropic surfaces: I. fundamentals and application to plane surface junctions*, *Surface Science*, 31 (1972), pp. 368–388.
- [19] Q.-A. HUANG, W. JIANG, AND J. Z. YANG, *An efficient and unconditionally energy stable scheme for simulating solid-state dewetting of thin films with isotropic surface energy*, *Commun. Comput. Phys.*, 26 (2019), pp. 1444–1470.
- [20] W. JIANG, W. BAO, C. V. THOMPSON, AND D. J. SROLOVITZ, *Phase field approach for simulating solid-state dewetting problems*, *Acta Mater.*, 60 (2012), pp. 5578–5592.
- [21] W. JIANG, Y. WANG, Q. ZHAO, D. J. SROLOVITZ, AND W. BAO, *Solid-state dewetting and island morphologies in strongly anisotropic materials*, *Scr. Mater.*, 115 (2016), pp. 123–127.
- [22] W. JIANG AND Q. ZHAO, *Sharp-interface approach for simulating solid-state dewetting in two dimensions: a Cahn–Hoffman ξ -vector formulation*, *Physica D*, 390 (2019), pp. 69–83.
- [23] W. JIANG, Q. ZHAO, AND W. BAO, *Sharp-interface model for simulating solid-state dewetting in three dimensions*, *SIAM J. Appl. Math.*, 80 (2020), pp. 1654–1677.
- [24] W. JIANG, Q. ZHAO, T. QIAN, D. J. SROLOVITZ, AND W. BAO, *Application of Onsager’s variational principle to the dynamics of a solid toroidal island on a substrate*, *Acta Mater.*, 163 (2019), pp. 154–160.

- [25] W. KAN AND H. WONG, *Fingering instability of a retracting solid film edge*, *J. Appl. Phys.*, 97 (2005), p. 043515.
- [26] G. H. KIM, R. V. ZUCKER, J. YE, W. C. CARTER, AND C. V. THOMPSON, *Quantitative analysis of anisotropic edge retraction by solid-state dewetting of thin single crystal films*, *J. Appl. Phys.*, 113 (2013), p. 043512.
- [27] O. KOVALENKO, S. SZABÓ, L. KLINGER, AND E. RABKIN, *Solid state dewetting of polycrystalline Mo film on sapphire*, *Acta Mater.*, 139 (2017), pp. 51–61.
- [28] U. F. MAYER, *Numerical solutions for the surface diffusion flow in three space dimensions*, *Comput. Appl. Math.*, 20 (2001), pp. 361–379.
- [29] J. MIZSEI, *Activating technology of SnO_2 layers by metal particles from ultrathin metal films*, *Sensor Actuat B-Chem.*, 16 (1993), pp. 328–333.
- [30] W. W. MULLINS, *Theory of thermal grooving*, *J. Appl. Phys.*, 28 (1957), pp. 333–339.
- [31] M. NAFFOUTI, R. BACKOFEN, M. SALVALAGLIO, T. BOTTEIN, M. LODARI, A. VOIGT, T. DAVID, A. BENKOUDER, I. FRAJ, L. FAVRE, ET AL., *Complex dewetting scenarios of ultrathin silicon films for large-scale nanoarchitectures*, *Sci. Adv.*, 3 (2017), p. eaao1472.
- [32] M. NAFFOUTI, T. DAVID, A. BENKOUDER, L. FAVRE, A. DELOBBE, A. RONDA, I. BERBEZIER, AND M. ABBARCHI, *Templated solid-state dewetting of thin silicon films*, *Small*, 12 (2016), pp. 6115–6123.
- [33] O. PIERRE-LOUIS, A. CHAME, AND Y. SAITO, *Dewetting of ultrathin solid films*, *Phys. Rev. Lett.*, 103 (2009), p. 195501.
- [34] P. POZZI, *Anisotropic mean curvature flow for two-dimensional surfaces in higher codimension: a numerical scheme*, *Interface Free Bound.*, 10 (2008), pp. 539–576.
- [35] E. RABKIN, D. AMRAM, AND E. ALSTER, *Solid state dewetting and stress relaxation in a thin single crystalline Ni film on sapphire*, *Acta Mater.*, 74 (2014), pp. 30–38.
- [36] S. RANDOLPH, J. FOWLKES, A. MELECHKO, K. KLEIN, H. MEYER III, M. SIMPSON, AND P. RACK, *Controlling thin film structure for the dewetting of catalyst nanoparticle arrays for subsequent carbon nanofiber growth*, *Nanotechnology*, 18 (2007), p. 465304.
- [37] S. RATH, M. HEILIG, H. PORT, AND J. WRACHTRUP, *Periodic organic nanodot patterns for optical memory*, *Nano Lett.*, 7 (2007), pp. 3845–3848.
- [38] D. J. SROLOVITZ AND S. A. SAFRAN, *Capillary instabilities in thin films: I. Energetics*, *J. Appl. Phys.*, 60 (1986), pp. 247–254.
- [39] D. J. SROLOVITZ AND S. A. SAFRAN, *Capillary instabilities in thin films: II. Kinetics*, *J. Appl. Phys.*, 60 (1986), pp. 255–260.
- [40] C. V. THOMPSON, *Solid-state dewetting of thin films*, *Annu. Rev. Mater. Res.*, 42 (2012), pp. 399–434.
- [41] Y. WANG, W. JIANG, W. BAO, AND D. J. SROLOVITZ, *Sharp interface model for solid-state dewetting problems with weakly anisotropic surface energies*, *Phys. Rev. B*, 91 (2015), p. 045303.
- [42] H. WONG, P. VOORHEES, M. MIKSIS, AND S. DAVIS, *Periodic mass shedding of a retracting solid film step*, *Acta Mater.*, 48 (2000), pp. 1719–1728.
- [43] J. YE AND C. V. THOMPSON, *Mechanisms of complex morphological evolution during solid-state dewetting of single-crystal nickel thin films*, *Appl. Phys. Lett.*, 97 (2010), p. 071904.
- [44] J. YE AND C. V. THOMPSON, *Anisotropic edge retraction and hole growth during solid-state dewetting of single crystal nickel thin films*, *Acta Mater.*, 59 (2011), pp. 582–589.
- [45] Q. ZHAO, W. JIANG, AND W. BAO, *An energy-stable parametric finite element method for simulating solid-state dewetting*, *IMA J. Num. Anal.*, (2020), doi:10.1093/imanum/draa070.
- [46] Q. ZHAO, W. JIANG, AND W. BAO, *A parametric finite element method for solid-state dewetting problems in three dimensions*, *SIAM J. Sci. Comput.*, 42 (2020), pp. B327–B352.
- [47] R. V. ZUCKER, G. H. KIM, W. C. CARTER, AND C. V. THOMPSON, *A model for solid-state dewetting of a fully-faceted thin film*, *C. R. Physique*, 14 (2013), pp. 564–577.